

An HST/COS legacy survey of intervening Si III absorption in the extended gaseous halos of low-redshift galaxies *

P. Richter^{1,2}, B.P. Wakker³, C. Fechner¹, P. Herenz¹, T. Tepper-García⁴, and A.J. Fox⁵

¹ Institut für Physik und Astronomie, Universität Potsdam, Karl-Liebknecht-Str. 24/25, 14476 Golm, Germany

² Leibniz-Institut für Astrophysik Potsdam (AIP), An der Sternwarte 16, 14482 Potsdam, Germany

³ Department of Astronomy, University of Wisconsin-Madison, 475 North Charter Street, Madison, WI 53706, USA

⁴ Sydney Institute for Astronomy, School of Physics, University of Sydney, NSW 2006, Australia

⁵ Space Telescope Science Institute, 3700 San Martin Drive, Baltimore, MD 21218, USA

Received 23/07/2015; accepted 10/03/2016

ABSTRACT

Aims. Doubly ionized silicon (Si III) is a powerful tracer of diffuse ionized gas inside and outside of galaxies. It can be observed in the local Universe in ultraviolet (UV) absorption against bright extragalactic background sources. We here present an extensive study of intervening Si III-selected absorbers and study the properties of the warm circumgalactic medium (CGM) around low-redshift ($z \leq 0.1$) galaxies.

Methods. We analyzed the UV absorption spectra of 303 extragalactic background sources, as obtained with the Cosmic Origins Spectrograph (COS) on-board the *Hubble Space Telescope* (HST). We developed a geometrical model for the absorption-cross section of the CGM around the local galaxy population and compared the observed Si III absorption statistics with predictions provided by the model. We also compared redshifts and positions of the absorbers with those of $\sim 64,000$ galaxies using archival galaxy-survey data to investigate the relation between intervening Si III absorbers and the CGM.

Results. Along a total redshift path of $\Delta z \approx 24$, we identify 69 intervening Si III systems that all show associated absorption from other low and high ions (e.g., H I, Si II, Si IV, C II, C IV). We derive a bias-corrected number density of $dN/dz(\text{Si III}) = 2.5 \pm 0.4$ for absorbers with column densities $\log N(\text{Si III}) > 12.2$, which is ~ 3 times the number density of strong Mg II systems at $z = 0$. This number density matches the expected cross section of a Si III absorbing CGM around the local galaxy population with a mean covering fraction of $\langle f_c \rangle = 0.69$. For the majority (~ 60 percent) of the absorbers, we identify possible host galaxies within 300 km s^{-1} of the absorbers and derive impact parameters $\rho < 200 \text{ kpc}$, demonstrating that the spatial distributions of Si III absorbers and galaxies are highly correlated.

Conclusions. Our study indicates that the majority of Si III-selected absorbers in our sample trace the CGM of nearby galaxies within their virial radii at a typical covering fraction of ~ 70 percent. We estimate that diffuse gas in the CGM around galaxies, as traced by Si III, contains substantially more (more than twice as much) baryonic mass than their neutral interstellar medium.

Key words. Keywords should be given

1. Introduction

Galaxies at low and high redshift are surrounded by massive gaseous halos. These halos are believed to be built up and fed by large-scale gas circulation processes, such as accretion from the intergalactic medium (IGM), galactic winds, and outflows powered by star formation and active galactic nuclei, as well as minor and major mergers that result from the on-going hierarchical formation and evolution of galaxies. Such gaseous material in extended galaxy halos is nowadays often referred to as the circumgalactic medium (CGM). We here define the CGM as diffuse neutral and ion-

ized gas that is located within the virial radius of a galaxy, but outside of its (main) stellar body.

Observational and theoretical studies imply that the CGM is a key component in the ongoing process of galaxy formation and evolution. Because the gas-consumption timescales of late-type galaxies are short compared to their lifetimes, they must gain gaseous material from outside (e.g., from the IGM and/or from merger processes) through the CGM to sustain their ongoing star formation. The manner in which the gas makes its way from the IGM/CGM to the disks of late-type spirals is not well understood, however. The classical picture of accretion (e.g., Rees & Ostriker 1977; White & Rees 1978; Birnboim & Dekel 2003) and the "hot-" and "cold-mode" scenarios (Kereš et al. 2005) most likely are oversimplified, because the underlying physics that describe the large-scale flows of multiphase gas from the outer to the inner regions of a dynamically evolving galaxy is highly complicated (e.g., Mo & Miralda-Escude 1996; Maller & Bullock 2004). Most likely, only state-of-

Send offprint requests to: P. Richter

e-mail: prichter@astro.physik.uni-potsdam.de

* Based on observations obtained with the NASA/ESA Hubble Space Telescope, which is operated by the Space Telescope Science Institute (STScI) for the Association of Universities for Research in Astronomy, Inc., under NASA contract NAS5D26555.

the art hydrodynamical simulations that cover the necessary physics and that have the necessary spatial resolution to potentially provide realistic measures for the amount of gas that is reaching the disk of late-type galaxies and for the timescales that it requires to do so (e.g., van de Voort et al. 2011).

Observations that aim at studying the properties of the CGM are thus extremely important to improve our understanding of gas-accretion processes and provide constraints for numerical models. What observations can provide is a characterization of the distribution of the different gas phases in the CGM, the total mass that it contains (under reasonable assumptions), and the connection between the properties of the CGM and the properties of their host galaxies (e.g., morphology, luminosity, star-formation rate, etc.). The gas densities in the CGM are low, however, so that emission measurements of circumgalactic gas (e.g., in the X-ray regime) typically are limited to the very inner halo regions of nearby galaxies using current instruments (Anderson & Bregman 2011; Dai et al. 2012; Bogdán et al. 2013). Fortunately, absorption-line measurements that use background active galactic nuclei (AGNs; throughout the following we use the abbreviation QSO to refer to the various classes of AGNs collectively) can access physical tracers at the relevant densities with extremely high sensitivity. For such absorption-line measurements the ultraviolet (UV) range is particularly important, as it contains a large number of diagnostic transitions from low, intermediate and high ions of heavy elements and the Lyman series of neutral hydrogen. Consequently, UV absorption-line observations with past and present space-based UV spectrographs such as the Far-Ultraviolet Spectroscopic Explorer (*FUSE*), the Space Telescope Imaging Spectrograph (STIS) and the Cosmic Origins Spectrograph (COS; the latter two instruments installed on the *Hubble Space Telescope*; *HST*) provide a wealth of information on the physical and chemical properties of the different gas phases in the CGM of the Milky Way and other galaxies (e.g., Wakker et al. 1999, 2001; Sembach et al. 2003; Richter et al. 2001, 2009, 2011; Tripp et al. 2003; Fox et al. 2005, 2010; Collins et al. 2009; Wakker & Savage 2009; Shull et al. 2009; Prochaska et al. 2011; Tumlinson et al. 2011; Lehner et al. 2013; Keeney et al. 2013; Werk et al. 2013; Stocke et al. 2014; Liang & Chen 2014).

In two previous papers, we have studied the amount and distribution of neutral gas (the so-called high-velocity clouds) in the halos of low redshift galaxies via optical absorption spectroscopy and their contribution to the neutral-gas accretion rate in the local Universe (Richter et al. 2011; Richter 2012). We here continue our long-term strategy to study the circumgalactic medium in the local Universe with an absorption-line survey that aims at characterizing the extent and mass of diffuse ionized gas around low-redshift galaxies using archival UV absorption-line data from *HST*/COS.

This paper is organized as follows. A short discussion on the importance of doubly ionized silicon as a sensitive tracer for circumgalactic gas is presented in Sect. 2. In Sect. 3 we describe the *HST*/COS data acquisition, the COS data reduction, the spectral analysis method, and the galaxy data origin. In Sect. 4 we discuss the observed absorber properties, such as their incident rate, their redshift distribution, the distribution of equivalent widths and column densities. In Sect. 5 we model the expected absorption cross section of

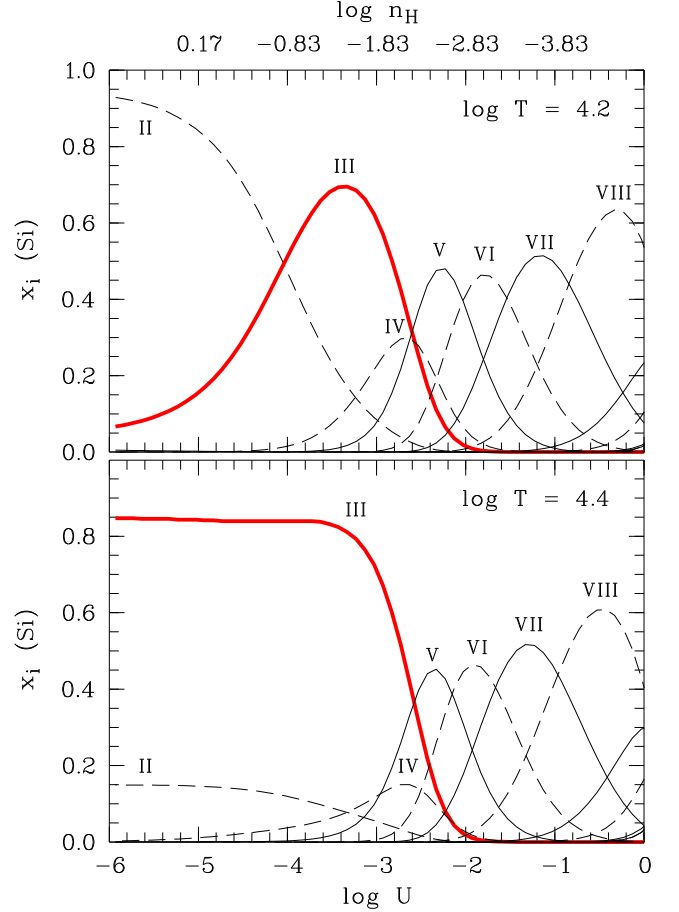


Fig. 1. Ionization fractions of different Si ionization states for different gas densities and temperatures, as calculated from a Cloudy ionization model (including photoionization and collisional ionization) of circumgalactic gas at $z = 0$ using the local UV background. The upper panel shows a model for $\log T = 4.2$, the lower panel a model for $\log T = 4.4$. The Si III ion represents the dominant ionization state in the density range that is characteristic for circumgalactic gas structures that are embedded in hot coronal gas ($\log n_H = -2.0$ to -3.5).

circumgalactic gas using the local galaxy luminosity function. Sect. 6 deals with the observed absorber-galaxy connection in our data sample. The ionization conditions and the cosmological mass density of the Si III absorbers are considered in Sect. 7. We discuss our results in Sect. 8 and provide a summary of our study in Sect. 9.

2. On the importance of Si III as a tracer of circumgalactic gas

A particularly powerful transition in the UV to detect ionized interstellar, circumgalactic, and intergalactic gas in a wide range of physical conditions is that of doubly ionized silicon (Si III) at 1206.500 Å (hereafter referred to as Si III $\lambda 1206$). This is because of the very high oscillator strength of Si III $\lambda 1206$ of $f = 1.63$ (Morton 2003) and the relatively large cosmic abundance of silicon ($\log (\text{Si}/\text{H})_{\odot} = -4.49$; Asplund et al. 2009). Doubly ionized silicon is a Mg-like ion with a closed-subshell $3s^2$ valence-

electron structure. The ionization-energy boundaries of the Si III ion are 16.35 and 33.49 eV (Morton 2003). As a result, detectable Si III arises from both diffuse photoionized as well as collisionally ionized gas at moderate temperatures ($T < 10^5$ K; see Shull et al. 2009).

To demonstrate the diagnostic power of the Si III $\lambda 1206$ transition for the study of the CGM we show in Fig. 1 the expected fractional abundance of the Si ions Si II–Si VIII in gas at $z = 0$ that is exposed to the local UV background. For the UV background we use a modified version of the model by Haardt & Madau (2012), in which we re-scale the photoionization rate to a value of $\log \Gamma = -13.6$ to compensate for the apparent discrepancies between the Haardt & Madau model and recent observational results (see Kollmeier et al. 2014; Wakker et al. 2015; Shull et al. 2015). The calculations (Fechner 2016, in prep.) are based on ionization models performed with the ionization code Cloudy (v13.03; Ferland et al. 2013). As can be seen, doubly ionized Si represents the dominant observable ionization state of Si at densities and temperatures ($\log n_{\text{H}} = -2.0$ to -3.5 , $T < 10^5$ K) that are typical for multiphase circumgalactic gas structures that are embedded in hot coronal gas (see Cen 2013).

In terms of quasar absorption-line systems, Si III $\lambda 1206$ absorption in the low-redshift Universe is expected to be detectable (if not blended by other spectral features) in basically *all* damped Lyman α absorbers (DLAs; $\log N(\text{H I}) \geq 20.3$), sub-damped Lyman α absorbers (sub-DLAs; $19.0 \leq \log N(\text{H I}) < 20.3$), Lyman-limit systems (LLS; $17.2 \leq \log N(\text{H I}) < 19.0$), because these are metal-enriched, multiphase absorbers with high gas columns. The majority of Si III-selected absorbers (throughout the following referred to simply as Si III absorbers), however, are expected to arise in ionized metal systems at lower H I column densities ($\log N(\text{H I}) < 17.2$), where the minimum H I column density to detect Si III with *HST*/COS in solar-metallicity gas at moderate gas densities ($n_{\text{H}} \sim 10^{-3} \text{ cm}^{-3}$) can be as low as $\log N(\text{H I}) = 14$ (see Sect. 7.1).

Low ions with lines in the observable UV, such as O I, C II, and Si II, are only present in mostly neutral or slightly ionized gas (i.e., at high $N(\text{H I})$), while high ions such as C IV and O VI predominantly trace highly-ionized gas at gas densities that are typically below $n_{\text{H}} \sim 10^{-3} \text{ cm}^{-3}$. A Si III-selected absorption-line survey, such as presented in this paper, therefore is expected to be particularly sensitive to detect metal-enriched gas in the inner and outer halos of galaxies and to characterize its spatial distribution and physical properties.

3. Observations, data handling, and analysis method

3.1. COS spectra selection and data reduction

For our study we make use of archival *HST*/COS data that were retrieved from the HST Science Archive at the Canadian Astronomy Data Centre (CADC). Because we aim at studying intervening Si III $\lambda 1206$ absorption in the IGM at $z \leq 0.1$ together with corresponding H I Ly α $\lambda 1215$ absorption we are primarily interested in the wavelength range between 1208 and 1338 Å. This range is covered by the COS G130M grating which operates between $\lambda = 1150 - 1450$ Å, providing a spectral resolution of $R \approx 15,000 - 20,000$ (corresponding to an instrumental

FWHM of $15 - 20 \text{ km s}^{-1}$, while the native pixel size is 2 km s^{-1} ; Green et al. 2012; Debes et al. 2016). Using the CADC web interface we searched for all publicly available COS data from all types of extragalactic point sources such as the various types of AGN and galaxies that were observed with the COS G130M grating. By the end of February 2014 we found (and downloaded) G130M data sets for 552 extragalactic sightlines. Whenever G160M data (covering the range $\lambda = 1405 - 1775$ Å including the important C IV doublet at 1548.2, 1550.8 Å) were available for these sightlines, we retrieved them as well.

For the further data reduction we used the raw COS spectra of the individual science exposures. The individual exposures were processed with the CALCOS pipeline (v2.17.3) to produce the standard COS x1d fits files. For the coaddition of the individual spectra we then used a custom-written code that aligns the individual exposures in wavelength space in a fully automated fashion. The code calculates for each exposure a pixel/wavelength calibration based on the line flanks (for spectra with $S/N > 5$) or line centers (for spectra with $S/N \leq 5$) of various interstellar anchor lines that are distributed over the wavelength range of the G130M and G160M spectral ranges. The heliocentric velocity positions of the anchor lines were calibrated for each sightline using H I 21cm data from the Leiden-Argentine-Bonn (LAB) survey (Kalberla et al. 2005). The individual spectra then were uniformly rebinned and coadded pixel-by-pixel (using the count rate in each pixel), where pixels with known artifacts were flagged accordingly. Errors were calculated in the coadded spectra by weighting by inverse variance. In this way, we obtained for each sightline a calibrated, co-added G130M spectrum (and G160M spectrum, if available). For each sightline we checked the quality of the data reduction by a visual inspection of the final spectrum.

As it turns out, many of the data sets have very low signal-to-noise ratios (S/N) and/or sample background sources with very low redshifts. These spectra are thus not suited to investigating intervening metal absorption at $z \leq 0.1$. We selected only those spectral data that have a minimum S/N per resolution element of four in the wavelength range between 1208 and 1338 Å and for which the redshift of the background source is $z_{\text{QSO}} > 0.03$. This selection reduces the total sample to 303 lines of sight (LOS). In Tables A.1–A.4 in the Appendix we present a complete list of all 303 QSO sightlines in our COS sample including QSO names and coordinates.

3.2. Redshift-path coverage, absorber identification, and spectral analysis

The next step in our analysis was to characterize the available redshift path to detect intervening Si III+H I Ly α absorption at $z \leq 0.1$ in each spectrum. We generally exclude the velocity range between $|v_{\text{helio}}| = 0 - 500 \text{ km s}^{-1}$ where absorption by local disk gas and by intermediate- and high-velocity clouds in the Milky Way halo is found (see, e.g., Wakker & van Woerden 1998; Richter 2006; Shull et al. 2009; Lehner et al. 2012; Putman, Peek & Joungh 2012; Herenz et al. 2013). To sort out regions that may be associated with the background AGN we further ignore the spectral range that lies within 5000 km s^{-1} of z_{QSO} . Finally, we identify and flag along each sightline those spectral regions that are heavily blended by other intervening absorbers (in

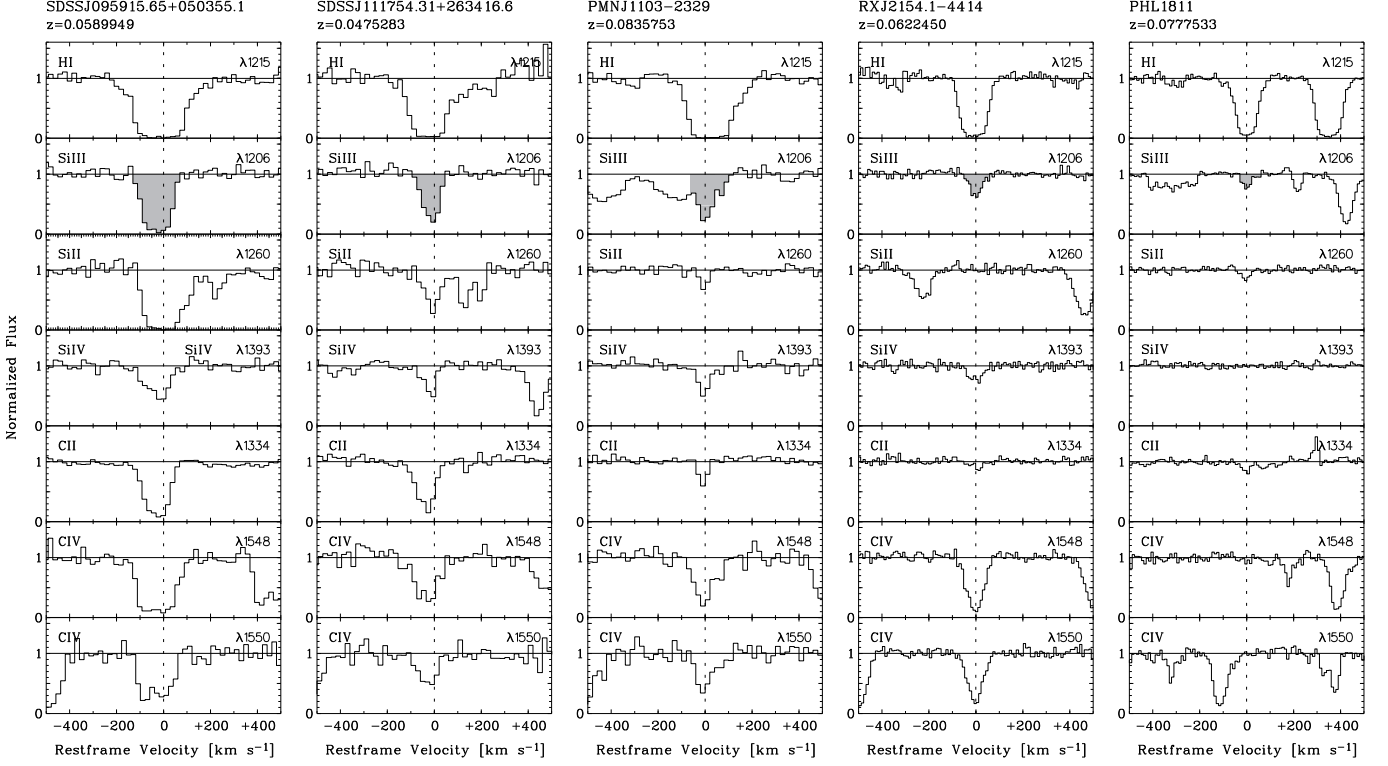


Fig. 2. Five examples for velocity profiles of Si III-selected absorption line systems in our *HST*/COS survey with decreasing Si III $\lambda 1206$ absorption strengths (gray-shaded area; from left to right). Shown are the velocity profiles of H I, Si III, Si II, Si IV, C II, and C IV (from top to bottom) plotted against the absorber’s restframe velocity. The names of the background QSOs and the absorption redshifts are indicated above each panel. A complete set of velocity plots for all detected Si III absorbers discussed in this paper is available in the Appendix.

particular by higher-redshift LLS and DLAs). As a result, we obtain a total absorption redshift path $\Delta z_{\text{abs}} < 0.1$ for each sightline that is available to identify intervening Si III+H I Ly α absorption (see Tables A.1-A.4, last column).

For the determination of the Si III number density (Sect. 4.2) we further need to consider the detection limit for Si III absorption along each sightline, which depends on the S/N in the relevant part of the spectrum where intervening Si III absorption is expected to occur. The minimum column density, N_{lim} , that can be detected at 3σ significance from an unresolved absorption line with a laboratory wavelength λ_0 and an oscillator strength f in a spectrum with a resolving power R and a given S/N per resolution element is given by (e.g., Richter et al. 2001; Tumlinson et al. 2002):

$$N_{\text{lim}} \approx 1.13 \times 10^{20} \frac{3}{R(S/N)f(\lambda_0/A)} \text{ cm}^{-2}. \quad (1)$$

For the only available Si III transition in the UV range we have $\lambda_0 = 1206.500 \text{ \AA}$ and $f = 1.62732$ (Morton 2003), so that for a S/N of 4 per resolution element the formal 3σ detection limit for $R = 15,000$ is $\log N_{\text{lim}}(\text{Si III}) = 12.46$. More than half of the considered COS spectra have a S/N per resolution element of ≥ 12 , so that for these LOS $\log N_{\text{lim}}(\text{Si III}) \leq 12.0$.

For the identification of intervening Si III absorbers at $z \leq 0.1$ in our COS data sample we used the following strategy. In a first step, we let an automated line-finder algorithm identify absorption features whose wavelengths would

correspond to combined Si III/H I Ly α absorption and created a candidate list of possible Si III absorbers. In a second step, we inspected each individual spectrum by eye and created a different (independent) candidate list. For each of the candidates from both lists velocity plots (including all relevant low and high ions in the available wavelength range) were generated and the absorber candidates were analyzed in detail. To meet our selection criteria of a bona fide Si III absorber, we require the significant detection of Si III and H I *together* with the detection of at least one additional metal ion (C IV, C II, Si IV, Si II) to avoid mis-identifications and false detections due to absorption features of other intervening absorbers at higher redshifts. Si III traces both diffuse ionized gas (as also traced by high ions such as C IV and Si IV) as well as denser, partly neutral gas (as also traced by singly-ionized species such as Si II and Mg II; see Fig. 1), so that the simultaneous detection of Si III with either one of the above listed low and high ions is expected.

We also identified a number of absorber candidates, that possibly show absorption in H I and Si III but lack absorption from any other ion, so that a unambiguous identification cannot be given.

For each intervening Si III absorber we checked for associated absorption in other metal ions (in particular Si II, Si IV, C II, C IV, N V, Fe II). We then measured equivalent widths (and their limits) for the strongest lines of the three different ionization states of silicon (Si II $\lambda 1260$, Si III $\lambda 1206$, Si IV $\lambda 1393$), C II $\lambda 1334$, and C IV $\lambda 1548$, as well as for H I Ly α by a direct pixel integration. Because of

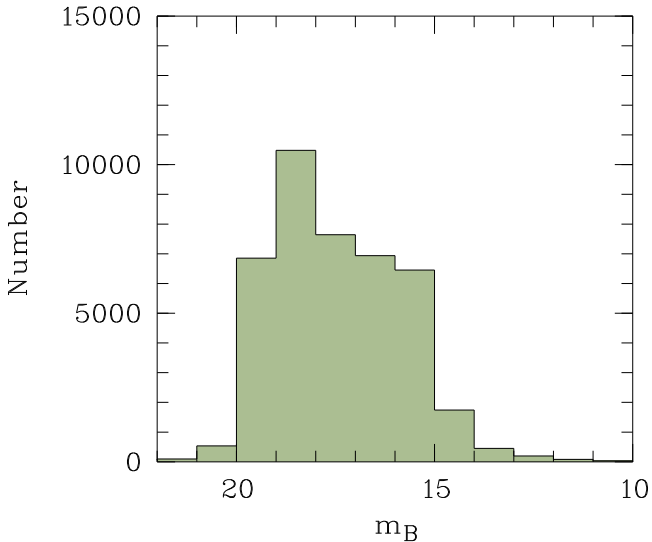


Fig. 3. Distribution of B band magnitudes for $\sim 41,000$ galaxies in our sample.

the limited spectral resolution and S/N of the COS data and the resulting lack of information about the intrinsic component structure in the absorbers we refrain from performing line fits for the analysis of the metal absorption in the systems. We instead use the apparent-optical depth method (AOD method; Savage & Sembach 1991) to derive column densities for unsaturated absorption in the above-listed lines and lower limits for lines that appear to be saturated. We assume that saturation becomes important for lines that have an absorption depth > 0.3 at the resolution of COS. Only for a small number of absorbers do we use Voigt-profile fitting to estimate the total H I column density from the damping wings of the H I Ly α absorption. The AOD method and Voigt-profile fitting are implemented in the custom-written `span` software package that is based on ESO-MIDAS and its data-reduction libraries (Fontana & Ballester 1995). Laboratory wavelengths and oscillator strengths for all ions were adopted from the compilation by Morton (2003).

3.3. Galaxy data

To statistically investigate the relation between Si III absorbers and low-redshift galaxies we searched for publicly available galaxy data in the SIMBAD data archive¹. Using SIMBAD we generated a list of galaxies with known redshifts located at $z \leq 0.1$ and within 2 deg of each sightline. A redshift of $z = 0.1$ corresponds to a proper distance of 420.9 Mpc at $z = 0.1$ for a standard Λ CDM cosmology with $\Omega_\Lambda = 0.72$, $\Omega_m = 0.28$ and $H_0 = 69.7 \text{ km s}^{-1} \text{ Mpc}^{-1}$ (Hinshaw et al. 2013²). In this way, we obtained redshifts and coordinates for 64,280 galaxies distributed around the 303 COS sightlines. For 40,907 of these galaxies we have additional information on their B -band magnitudes. The distribution of m_B for these systems is shown in Fig. 3. The distribution breaks down at $m_B = 20.0$, with only two

percent of the galaxies having $m_B > 20.0$. For $z = 0.1$ and the above given cosmology, $m_B = 20.0$ corresponds to an absolute magnitude of $M_B \approx -18.1$. If we consider the g -band SDSS galaxy-luminosity function (Montero-Dorta & Prada 2009) as reference, this value translates into a lower luminosity cutoff of $L \approx 0.5 L^*$.

For each sightline, we then calculated the projected impact parameters, ρ , of the galaxies to the LOS. There are 11,127 galaxies within $\rho = 1$ Mpc located in the cylindrical volume around the 303 sightlines. This number implies a mean galaxy density of $\phi \approx 0.03 \text{ Mpc}^{-3}$ in our total galaxy sample, which is about seven times the space density of L^* galaxies in SDSS g -band (Montero-Dorta & Prada 2009).

At this point it is important to mention that the galaxy catalog created in this way is highly inhomogeneous because the data stems from different galaxy surveys and pointed observations. As a result, the individual values for ϕ for each sightline vary considerably. In terms of luminosities, only a few sightlines have galaxy data that are sufficiently deep to detect faint ($L \leq 0.05 L^*$) galaxies. In general, our galaxy data is incomplete for $L < 0.5 L^*$. This aspect needs to be carefully taken into account for the interpretation of the observed absorber/galaxy relation. For many sightlines, we are missing low-luminosity galaxies that may be close to the LOS and/or responsible for the observed metal absorption (see discussion in Sect. 6). We do not consider any other morphological parameters of the selected galaxies (Hubble type, star-formation rate, etc.), because such information is available to us only for a small fraction of the galaxies in our sample.

4. Absorber properties

4.1. Si III detection rate, equivalent widths and column densities

Using the above outlined strategy, we identify 69 intervening Si III absorbers along the 303 selected QSO sightlines. The statistical and physical properties of these 69 intervening absorbers are discussed in this section.

In Tables A.5-A.10 in the Appendix we list the measured equivalent widths and derived column densities for the various ions detected in these systems. These tables also contain information on two additional strong metal absorbers towards SDSSJ141542.90+163413.8 and UKS-0242-724 that are detected in Si II, Si IV, and other ions, but not in Si III, because there are no useful data in the relevant spectral region where Si III is expected. In Fig. 2 we show five examples for velocity profiles of intervening Si III absorbers with different Si III absorption strengths. The complete set of velocity profiles for all 69 confirmed Si III absorbers is provided in Figs. A.1-A.7 in the Appendix of this paper. Following the criteria defined in the previous section we further identify 20 Si III candidate absorbers along the 303 lines of sight. Although these candidate systems are not considered in the further analysis, we list the QSO names and (possible) absorption redshifts of these systems in Table A.11 in the Appendix.

The redshift distribution of the 69 absorbers is shown in Fig. 4, left panel. The absorption redshifts lie between $z = 0.00014$ and $z = 0.09789$. While for $z = 0.01 - 0.10$ the absorbers are uniformly distributed over the surveyed redshift range, the distribution shows a peak in the first redshift bin at $z < 0.01$. This peak is related to an over-

¹ <http://simbad.u-strasbg.fr>

² These values are consistent at the 2σ level with the latest measured values by the Planck Collaboration (Planck Collaboration 2015. XIII).

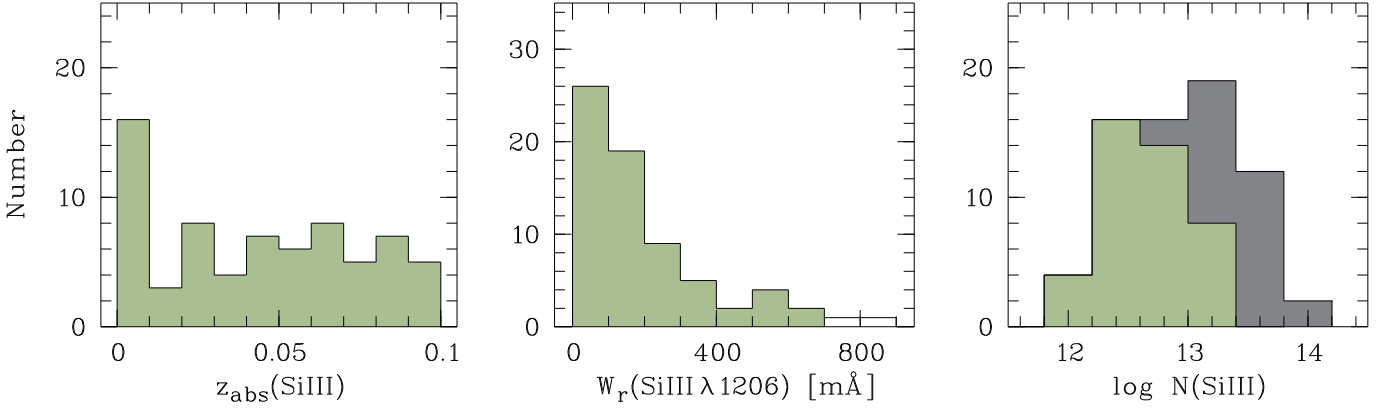


Fig. 4. *Left panel:* Redshift distribution of the 69 intervening Si III absorbers in our sample. *Middle panel:* Distribution of Si III $\lambda 1206$ restframe equivalent widths of the 69 absorbers, obtained from the pixel integration over the Si III velocity profiles. *Right panel:* Distribution of logarithmic Si III column densities for the 69 absorbers, derived using the AOD method. The gray-shaded area indicates lower limits for $\log N(\text{Si III})$ for absorbers that have saturated Si III $\lambda 1206$ lines.

density of Si III absorbers in the broader Virgo-Cluster environment that is traced along several sightlines in our QSO sample. In the middle panel of Fig. 4 we show the distribution of Si III $\lambda 1206$ equivalent widths of the 69 absorbers. The distribution peaks at relatively low equivalent widths ($W_r \leq 100$ mÅ); 65 percent of the absorbers have $W_r \leq 200$ mÅ, while most of the remaining 35 percent are spread over a large range in W_r between 200 and 700 mÅ. There are two systems that have very large equivalent widths of $W_r > 700$ mÅ, belonging to strong absorption systems towards SDSSJ140732.25+550725.6 and PG 0832+251 (see Appendix).

Si III column densities for the 69 absorbers, as derived from the AOD method (see previous section), are shown in the right panel of Fig. 4. The gray-shaded area (which adds to the green-shaded area) indicates lower limits of $N(\text{Si III})$ for absorbers where the Si III $\lambda 1206$ line shows evidence for saturation. The decline of the observed distribution at low column densities reflects both the inhomogeneous S/N in the spectra as well as the column density distribution that is intrinsic to the absorber population. From the estimate of $N_{\text{lim}}(\text{Si III})$ for each sightline (see equation 1) follows that more than 90 percent of all sightlines are sensitive to detect Si III absorbers with $\log N(\text{Si III}) < 12.2$, but only four such systems are found in our data (fractional abundance $4/69 \approx 0.04$). Therefore, intervening Si III absorbers with $\log N(\text{Si III}) < 12.2$ are rare and may even represent a population that is distinct from the absorbers with higher column densities (as is discussed later). At the high-column density end, the distribution breaks down at $\log N(\text{Si III}) = 14$. Even if some of the saturated absorbers (gray-shaded range) would have logarithmic Si III column densities > 14 , their number would be small compared to absorbers with $\log N(\text{Si III}) < 14$. Our conclusion is that the *characteristic* column density range for intervening Si III absorbers is $\log N(\text{Si III}) = 12.2 - 14.0$.

4.2. Number density of Si III absorbers

For the determination of the number density of intervening Si III absorbers per unit redshift, dN/dz , we need to con-

sider in detail the completeness of our absorber survey and the selection bias in our QSO sample.

As discussed above, $\log N_{\text{lim}}(\text{Si III}) \geq 12.2$ represents the column density range that is characteristic for intervening Si III absorbers. 63 Si III absorbers in our sample have column densities $\log N_{\text{lim}}(\text{Si III}) \geq 12.2$ and 280 out of the 303 sightlines are sensitive to this level, covering a total redshift path of $\Delta z_{\text{abs}} = 21.95$. The resulting number density thus is $dN/dz = 2.9 \pm 0.4$. The given errors represent statistical errors calculated from Poisson statistics. For $\log N_{\text{lim}}(\text{Si III}) = 11.8$ we derive $dN/dz = 4.0 \pm 0.7$ (31 absorbers, $\Delta z_{\text{abs,tot}} = 7.8$), while for $\log N_{\text{lim}}(\text{Si III}) = 12.6$ the number density is slightly smaller ($dN/dz = 2.1 \pm 0.3$, 49 absorbers, $\Delta z_{\text{abs,tot}} = 23.6$). If we consider only low-column density absorbers with $\log N(\text{Si III}) = 11.8 - 12.2$ we obtain $dN/dz \approx 0.3$.

One important effect that influences the observed frequency of intervening absorption systems is the selection bias in the QSO sample that we are using. Most of the bright QSOs in our COS sample have been previously studied using instruments such as *HST*/STIS, *FUSE*, and others. While the original motivation to select these background sources certainly was their intrinsic brightness, the re-observation of these sources with COS and the chosen integration time (e.g., the achieved S/N), possibly was motivated by targeting particularly interesting intervening absorbers to perform a detailed study of these systems. Therefore, one of the reasons for limiting the absorber sample to redshifts $z \leq 0.1$ was to avoid the inclusion of targeted observations of stronger intervening metal absorbers at $z > 0.12$ that can be observed in both H I Ly α as well as Ly β .

We have scanned the various original COS proposals that outline the motivation for observing the LOS along which we detect intervening Si III at $z \leq 0.1$. As it turns out, our QSO sample covers most of the sightlines selected for the COS-Dwarfs survey (Bordoloi et al. 2014), a targeted survey of sightlines passing through the virial radius of $z \leq 0.1$ dwarf galaxies to study the CGM of these systems. For an un-biased estimate of $dN/dz(\text{Si III})$ all these sightlines need to be excluded. All in all, we identify 40 QSO sightlines in our sample that have been specifically observed to study circumgalactic gas in the vicinity of known

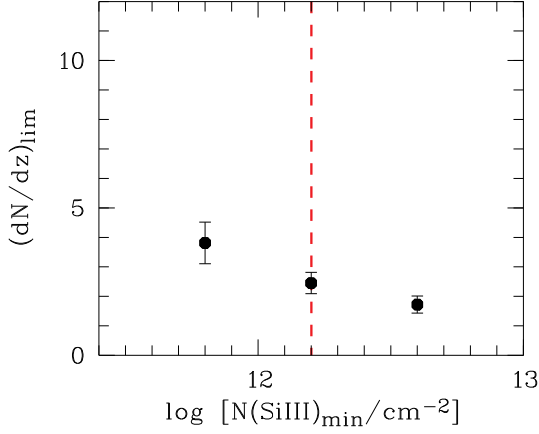


Fig. 5. Number densities, dN/dz , of intervening Si III absorbers for different limiting column densities.

low-redshift galaxies. By removing these sightlines from our sample we derive the following bias-corrected number densities of Si III absorbers for the different limiting Si III column densities: $dN/dz = 3.8 \pm 0.7$ for $\log N_{\text{lim}}(\text{Si III}) = 11.8$, $dN/dz = 2.5 \pm 0.4$ for $\log N_{\text{lim}}(\text{Si III}) = 12.2$, and $dN/dz = 1.7 \pm 0.3$ for $\log N_{\text{lim}}(\text{Si III}) = 12.6$. For the range $\log N(\text{Si III}) = 11.8 - 12.2$ we again obtain $dN/dz \approx 0.3$.

It is evident that these numbers are not substantially different from those derived from the biased sample. This is, however, not surprising because it is known that the UV absorption cross section of the warm CGM around *dwarf galaxies* appears to be small when compared to the warm CGM of more massive galaxies (e.g., Bordoloi et al. 2014; Liang & Chen 2014; see also Sect. 8.3). In other words: only a few *additional* Si III absorbers are (in a statistical sense) added to our absorber sample when including the pre-selected Bordoloi et al. sightlines, but because of the overall large size of our QSO sample their influence on dN/dz is small.

In Fig. 5 we show the bias-corrected number density of intervening Si III absorbers per unit redshift in our survey, dN/dz , for the three different limiting Si III column densities, $\log N_{\text{lim}}(\text{Si III}) = 11.8, 12.2$ (dashed red line), and 12.6. In the following, we refer to these values when discussing the number densities of intervening Si III absorbers.

4.3. Associated absorption from other ions

4.3.1. H I

As outlined in the introduction, the Si III ion is, because of its ionization potential, a very sensitive tracer for both predominantly neutral as well as predominantly ionized gas in the halos of galaxies. As a consequence, the H I column density in the Si III absorbing gas varies over several orders of magnitudes, ranging from $\log N(\text{H I}) \sim 14$ up to $\log N(\text{H I}) \sim 22$, depending on whether the sight line passes through a galaxy disk or a galaxy halo, and on the local ionization conditions. Detailed ionization models of the Si III absorbers are presented in Sect. 7. In the left panel of Fig. 6 we show the distribution of H I Ly α equivalent widths in the Si III-selected absorbers, which similarly span an extremely large range from $W_r \approx 250$ mÅ to $W_r \approx 5$ Å. We generally refrain from estimating the H I column densities

from the saturated H I Ly α lines because of the very large uncertainties that such an estimate would be afflicted with.

It is worth noting that our absorber sample contains four damped Ly α /sub-damped Ly α systems (DLAs/sub-DLAs) with $\log N(\text{H I}) > 19.2$, as estimated from fitting the damping wings of the Ly α absorption in these systems. With a total redshift path of $\Delta z_{\text{abs,tot}} = 21.95$, this absorber frequency corresponds to a number density of $dN/dz \approx 0.2$. Despite the low-number statistics, it is worth mentioning this value agrees well with the expected number density of sub-DLAs/DLAs as estimated from the H I mass function of $z \approx 0$ galaxies (Zwaan et al. 2005).

4.3.2. Si II

Detailed ionization models (see Sect. 7) indicate that regions with gas densities $\log n_{\text{H}} \geq -3.5$ and sufficiently large neutral hydrogen column densities are expected to show both Si III as well as Si II absorption. Because Si II and Mg II have almost identical ionization potentials (Morton 2003) and silicon and magnesium have similar solar abundances (Asplund et al. 2009), the absorber statistics for Si II can be directly compared with the well-established statistics on intervening Mg II absorbers. The presence of Si II absorption *without* associated Si III is basically impossible for any realistic galactic or circumgalactic gas environment (see Sect. 7), so that the fact that our absorber sample is Si III-selected is not expected to introduce a selection bias in our Si II statistics.

Fourty of our Si III absorbers show associated Si II absorption in the strongest of the available Si II lines at $\lambda_0 = 1260.42$ Å. The equivalent-width distribution for Si II $\lambda 1260$ in these absorbers is shown in the middle panel of Fig. 6. It shows that the majority (80 percent) of the detected Si II lines have equivalent widths in the $\lambda 1260$ line of < 300 mÅ. To compare the observed number density of Si II-bearing absorbers with that of the prominent strong Mg II systems, i.e., systems that have an equivalent width of $W_r \geq 300$ mÅ in the Mg II $\lambda 2976$ line, we need to convert the observed Si II $\lambda 1260$ equivalent widths into Mg II $\lambda 2976$ equivalent widths. For this we use the Si II/Mg II conversion scheme presented in Herenz et al. (2013), after which an equivalent widths of $W_r = 300$ mÅ in the Mg II $\lambda 2976$ line corresponds to an equivalent width of $W_r = 140$ mÅ in Si II $\lambda 1260$, assuming solar relative abundances of Mg and Si. In our absorber sample we have 22 systems that have $W_r \geq 140$ mÅ in the Si II $\lambda 1260$ line, from which we indirectly infer a number density of strong Mg II absorbers at $z \leq 0.1$ of $dN/dz \approx 1.0$. This value is in good agreement with the expectations for $dN/dz(\text{Mg II } \lambda 2976)$ based on the redshift evolution of strong Mg II absorbers in SDSS data ($dN/dz \sim 0.8$; Nestor, Turnshek & Rao 2005; Prochter et al. 2006; Lundgren et al. 2009; Zhu & Menard 2013).

4.3.3. Si IV

There are 38 Si III absorbers in our sample that show associated Si IV absorption (the two available Si IV transitions are located at $\lambda_0 = 1393.8$ and 1402.8 Å, the former being the stronger of the two transitions; Morton 2003). The distribution of Si IV $\lambda 1393$ equivalent widths of the 38 absorbers detected in Si IV is shown in the right panel of Fig. 6. Similarly as for Si II, the majority of the Si IV $\lambda 1393$ equivalent widths

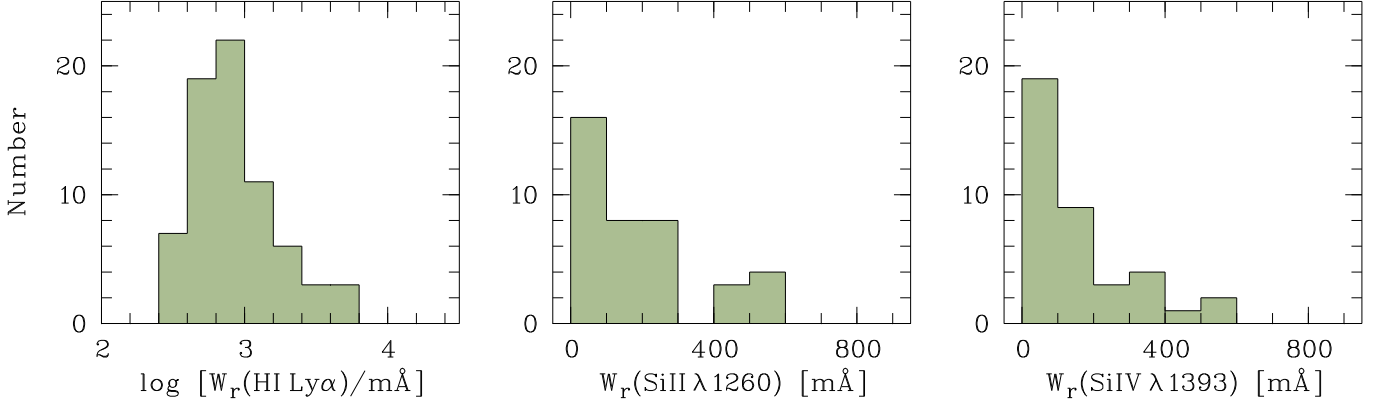


Fig. 6. Distribution of restframe equivalent widths of $\text{HI Ly } \alpha$ (*left panel*), $\text{Si II } \lambda 1260$ (*middle panel*), and $\text{Si IV } \lambda 1393$ (*right panel*) associated with intervening Si III absorbers.

are small (82 percent have $W_r(1393) < 300 \text{ m}\text{\AA}$). From the observed frequency of Si IV absorption in the Si III -selected systems we estimate $dN/dz(\text{Si IV}) \geq 1.5$ for $\log N(\text{Si IV}) \geq 12.6$. The occurrence of Si IV absorption *without* associated Si III absorption in the CGM/IGM is possible, in principle, but is relevant only for absorbers at relatively low gas densities ($\log n_{\text{H}} \leq -4.2$; see Sect. 7). Still, we formally can only give a lower limit for $dN/dz(\text{Si IV})$ from our survey.

4.4. Correlation plots

In Fig. 7 we show correlations between the measured (logarithmic) equivalent widths of $\text{Si III } \lambda 1206$, $\text{HI Ly } \alpha$, $\text{Si II } \lambda 1260$, and $\text{Si IV } \lambda 1393$ for absorbers in which the absorption in these ions is aligned in velocity space within one COS resolution element (20 km s^{-1}). The interpretation of the observed correlations involves the possible presence of different gas phases in the absorbers that may or may not be co-spatial within the overall gas structures.

4.4.1. Si III vs. HI

For $\log [W_r(\text{Ly } \alpha)] \leq 3$ the $\text{Si III } \lambda 1206$ equivalent width rises steeply with the mildly increasing equivalent width of the fully saturated $\text{HI Ly } \alpha$ absorption (Fig. 7; left panel). This trend indicates (as expected) that Si III and HI trace the same physical regions that span a large range in neutral (and total) gas column densities. For $\log [W_r(\text{Ly } \alpha)] > 3$ the correlation turns over into a somewhat flatter regime because the $\text{Si III } \lambda 1206$ absorption itself becomes saturated at such high total gas columns.

4.4.2. Si III vs. Si II

The equivalent widths of $\text{Si III } \lambda 1206$ and $\text{Si II } \lambda 1260$ clearly are correlated with each other in those absorbers, where both ions are detected (Fig. 7; second panel from left, filled circles). This demonstrates that part of the Si III arises in the same gas phase as Si II , i.e., in predominantly neutral and/or mildly ionized gas. Some of the systems with upper limits in $W_r(\lambda 1260)$ (open circles/arrows) have relatively strong Si III absorption without a Si II counterpart, implying

that these absorbers consist of predominantly ionized gas that is traced by higher ions (e.g., Si IV , see below).

4.4.3. Si III vs. Si IV

For systems that show both Si III as well as Si IV absorption the equivalent width of $\text{Si III } \lambda 1206$ is also correlated with that of $\text{Si IV } \lambda 1393$, as can be seen in the third panel of Fig. 7 (filled circles). This trend indicates that some part of the Si III resides in a more ionized gas phase that is traced by Si IV (and other high ions such as C IV). The relation is mildly steeper than the one for $\text{Si III}/\text{Si II}$, but has as similar level of scatter.

4.4.4. Si II vs. Si IV

In the right panel of Fig. 7 we have plotted the equivalent width of $\text{Si II } \lambda 1260$ against that of $\text{Si IV } \lambda 1393$ for the absorbers where both ions are detected. The total number of systems that show aligned Si II and Si IV absorption is relatively small (38 percent). This implies that both ions predominantly trace complementary gas phases. For the systems detected in both ions (filled circles) the correlation between $W_r(\text{Si II } \lambda 1260)$ and $W_r(\text{Si IV } \lambda 1393)$ is weak and shows a relatively large scatter.

4.4.5. Interpretation

We conclude that the correlation plots between the equivalent widths of $\text{Si III } \lambda 1206$, $\text{HI Ly } \alpha$, $\text{Si II } \lambda 1260$, and $\text{Si IV } \lambda 1393$ are in line with (and further support) the idea that the Si III absorption in intervening metal-systems traces metal-enriched gas within a wide range of physical conditions including a) a denser (partly neutral) phase also traced by Si II and other low ions, and b) a more diffuse (predominantly ionized) gas phase also traced by Si IV and other high ions. We further discuss these aspects in Sect. 7 where we model the ionization conditions in $\text{Si III}/\text{Si IV}$ absorbers in detail.

In a recent C IV -selected survey of absorbers at $z \leq 0.16$ Burchett et al. (2015) find very similar relations between Si II , Si III , and Si IV in their absorber sample (their Figs. 15 and 16).

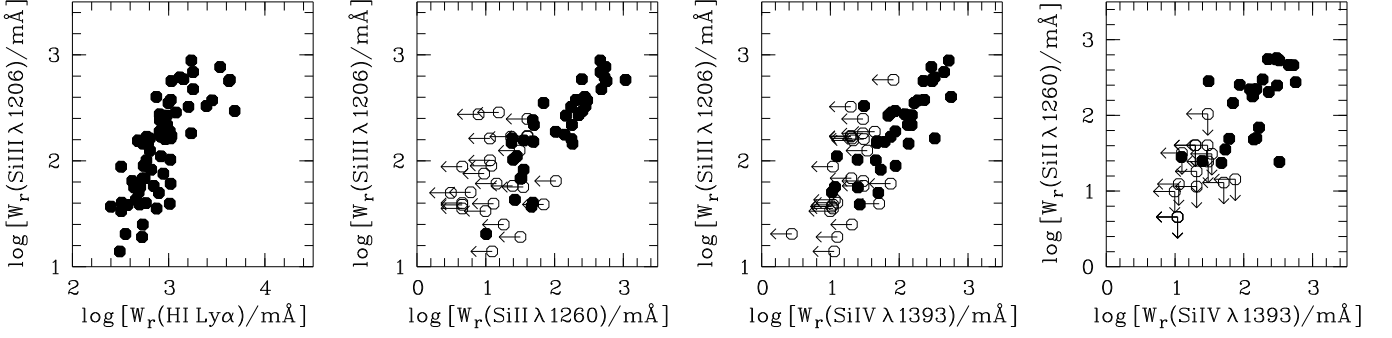


Fig. 7. Comparison between restframe equivalent widths of Si III, Si II, Si IV, and H I for 69 absorbers. *First panel (left):* Si III λ 1206 vs. H I Ly α ; *Second panel:* Si III λ 1206 vs. Si II λ 1260; *Third panel:* Si III λ 1206 vs. Si IV λ 1393; *Fourth panel:* Si II λ 1260 vs. Si IV λ 1393.

5. On the expected cross section of metal-enriched gas in galaxy halos

Before we investigate in detail the *observed* relation between Si III absorbers and galaxies in a statistical sense, we first set up a geometrical model to estimate the expected cross section of metal-enriched gas in the extended gaseous halos of galaxies at $z = 0$.

Under the assumption that *all* intervening Si III absorbers at low z are related to metal-enriched gas situated in the extended halos of galaxies, the observed number density of Si III absorbers can be directly linked to the space density of galaxies, ϕ , and the effective (geometrical) cross section of the absorbing gas, which is a product of the projected area covered by the gaseous halo $A_{\text{halo}} = \pi r_{\text{halo}}^2$ and the mean covering fraction $\langle f_c \rangle$ of the gas phase that is seen in absorption:

$$\frac{dN}{dz} = \phi \langle f_c \rangle A_{\text{halo}} \frac{c(1+z)^2}{H(z)}. \quad (2)$$

The Hubble parameter is defined as $H(z) = H_0 (\Omega_m (1+z)^3 + \Omega_\Lambda)^{1/2}$, which is appropriate for a matter-dominated flat Universe with a cosmological constant. Equation (2), and modified versions of it, have been commonly used to estimate the sizes of galaxy halos and the covering fractions of individual ions from QSO absorption-line observations (e.g., Kapzcrak et al. 2008; Richter et al. 2011; Prochaska et al. 2011).

We here take the opposite point of view and pose the following question: What would be the expected number density of intervening metal absorbers, if all galaxies at $z = 0$ contain detectable metal-enriched gas in their halos that extends exactly to their respective virial radii?

Using equation (2) it is indeed relatively straightforward to set up a “toy model” for the absorption cross section of extended halo gas taking into account the observed space density and luminosity/mass distribution of galaxies at low redshift. The motivation for such a reverse approach is rather simple: *if we could know the maximum contribution of metal-enriched gas that is gravitationally bound to galaxies to the number density of intervening metal absorbers, we would have an important reference value for the interpretation of the observed number densities of intervening Si III systems and their origin in the CGM and/or IGM.*

Both the galaxy density ϕ as well as the distribution of the galaxies’ virial radii at $z = 0$, i.e., the most important parameters to calculate dN/dz via equation (4), can be obtained indirectly from the local galaxy luminosity function. We here adopt the g -band SDSS luminosity function from Montero-Dorta & Prada (2009), who give Schechter parameters of $\alpha = -1.10$ and $\phi^* = 1.25 \times 10^{-2} h^3 \text{ Mpc}^{-3}$ for $h = 1.0$. We transform these parameters to the cosmological frame defined in Sect. 3.3. and calculate $\phi = \phi^* \Gamma(\alpha + 1, L/L^*)$ for different luminosity bins, where Γ is the incomplete gamma function and L^* is the characteristic luminosity that characterizes the cut-off for the power-law component in the Schechter luminosity function (Schechter 1976).

The key assumption in our toy model is that all halos of galaxies with luminosities $L \geq 0.001 L^*$ contain metal-absorbing gas within their virial radii (R_{vir}). We initially assume a unity covering fraction of the absorbing gas, so that the effective absorption cross section is simply πR_{vir}^2 . Also the virial radius of a galaxy can be inferred indirectly from its luminosity. As recently discussed by Stocke et al. (2014), halo matching models provide a relatively well-defined relation between R_{vir} and L that can be used to define a scaling relation between these two parameters. We define $C = \log(L/L^*)$ and approximate the relation between L and R_{vir} shown in Stocke et al. (their Fig. 8) by the fit

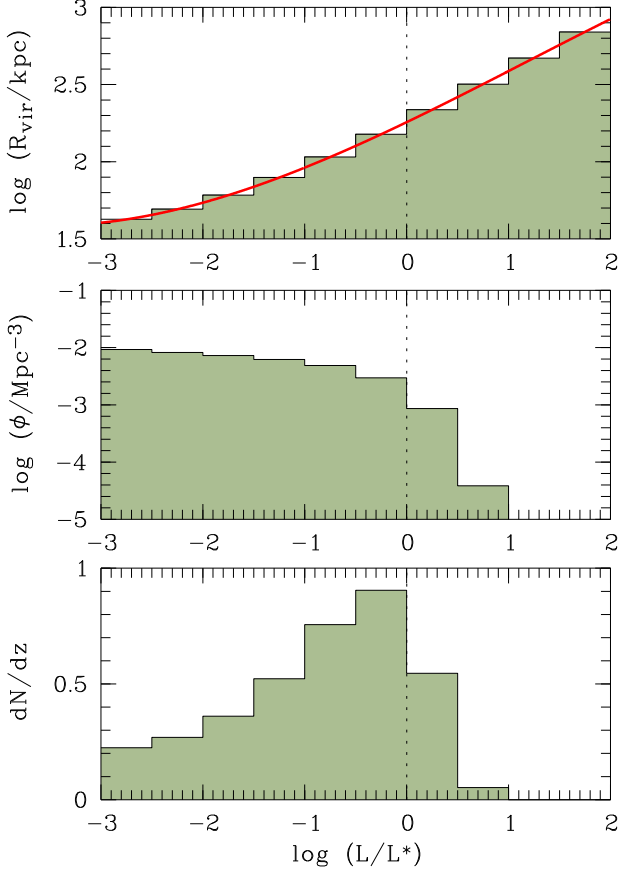
$$\log R_{\text{vir}} = 2.257 + 0.318 C + 0.018 C^2 - 0.005 C^3. \quad (3)$$

Equipped with these relations we can now assign to each luminosity bin a galaxy space density $\phi(L)$ and an effective absorption cross section $A(L) = \pi R_{\text{vir}}^2(L)$, which is all we need to calculate the expected number density of absorbers $dN/dz(L)$ for the same bin. Integration over all galaxy luminosity bins then provides the expected total number density of absorbers arising from the halos of these galaxies.

Fig. 8 summarizes the main results from our modeling. The red solid line in the upper panel visualizes the $L - R_{\text{vir}}$ -relation defined by equation (3), while the green-shaded histogram indicates the same relation in bins of $\log(L/L^*) = 0.5$. In the middle panel of Fig. 8 the logarithmic galaxy density ($\log \phi(L)$) is plotted against $\log(L/L^*)$ (same binning), while in the lower panel we show the expected number density of absorbers $dN/dz(L)$ (assuming a unity covering fraction, $\langle f_c \rangle = 1$) as a function of $\log(L/L^*)$ for the same binning. By integrating over the de-

Table 1. Models^a for absorber cross sections based on equation (2)

Model	α	ϕ_{\min}^* [$h^3 \text{ Mpc}^{-3}$]	ϕ_{pref}^* [$h^3 \text{ Mpc}^{-3}$]	ϕ_{\max}^* [$h^3 \text{ Mpc}^{-3}$]	dN/dz_{\min}	dN/dz_{pref}	dN/dz_{\max}
1	-1.00	0.0075	0.0125	0.0175	1.81	3.02	4.23
2	-1.10	0.0075	0.0125	0.0175	2.18	3.64	5.09
3	-1.20	0.0075	0.0125	0.0175	2.73	4.56	6.38
4	-1.30	0.0075	0.0125	0.0175	3.58	5.97	8.35

^aThe following Schechter parameters are given: α = slope of the power-law component; ϕ^* = normalization density; the preferred parameter combination is indicated with the bold-face font.

Fig. 8. Predictions from the halo model described in Sect. 5. *Upper panel:* The virial radius of galaxies as a function of galaxy luminosity (adapted from Stocke et al. 2014). *Middle panel:* Galaxy space density as a function of galaxy luminosity (from Montero-Dorta & Prada 2009). *Lower panel:* Expected number density of CGM absorbers as a function of galaxy luminosity.

sired luminosity range we obtain an estimate for the total number density of absorbers that arise in the gaseous halos of the galaxies in that luminosity range.

While our observational galaxy sample is restricted to relatively bright galaxies (see Sect. 3), we here consider the much larger range $L/L^* \geq 0.001$ to evaluate the potential contribution of faint galaxies and their halos to the total cross section of intervening metal absorbers, even if they remain unseen in galaxy surveys. For $L/L^* \geq 0.001$ and unity covering fraction we obtain a total absorber number density of $dN/dz = 3.6$. If we include the mean covering

fraction as free parameter (which then represents an area-weighted mean), we can write more generally:

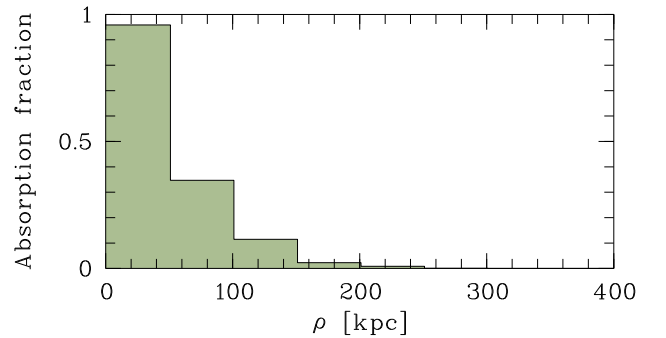
$$dN/dz = 3.6 \langle f_c \rangle. \quad (4)$$

For realistic gas covering fractions in galaxy halos in the range $\langle f_c \rangle = 0.1 - 1.0$ this absorber number density is remarkably close to the observed number density of intervening Si III absorbers, as discussed in the previous section.

Table 2. Model predictions for effective CGM covering fractions, $\langle \mathcal{F}_c(r_{\max}) \rangle$, for different halo radii and galaxy luminosities (see Sect. 5).

r_{\max} [kpc]	$\langle f_c \rangle$	$\langle \mathcal{F}_c(r_{\max}) \rangle$			
		$L/L^* \geq 0.001$	$L/L^* \geq 0.01$	$L/L^* \geq 0.1$	$L/L^* \geq 1$
200	1.00	0.18	0.27	0.48	1.00
400	1.00	0.04	0.07	0.12	0.31
1000	1.00	0.01	0.01	0.02	0.05
200	0.75	0.13	0.20	0.36	0.96
400	0.75	0.03	0.05	0.09	0.23
1000	0.75	0.01	0.01	0.01	0.04
200	0.50	0.09	0.14	0.24	0.62
400	0.50	0.02	0.03	0.06	0.16
1000	0.50	0.00	0.01	0.01	0.02

One serious concern about the relevance of the above given estimate is, how strongly the derived absorber number density depends on the input parameters from the adopted galaxy luminosity function. To explore this dependence we have calculated dN/dz for a whole set of (realistic) Schechter parameters, as presented in Table 1. For this, we vary for a given slope α in each row the normalization density from ϕ_{\min}^* over ϕ_{pref}^* to ϕ_{\max}^* (where


Fig. 9. CGM absorption fraction as a function of impact parameter, as predicted from the halo model described in Sect. 5.

$\phi_{\text{pref}}^* = 0.0125 h^3 \text{ Mpc}^{-3}$ represents our preferred normalization; see above) and calculate the expected absorber number densities dN/dz_{min} , dN/dz_{pref} , dN/dz_{max} . For Schechter parameters in the range $\alpha = [-1.0, -1.3]$ and $\phi^* = [0.0075, 0.150]$ the expected number densities vary between $dN/dz = 1.81$ and 8.35 . It is therefore valid to claim that the expected contribution of the metal-enriched CGM to the cross section of intervening metal absorbers is $dN/dz < 9$ (this conclusion holds for any metal ion that can be observed via QSO absorption spectroscopy).

One may argue that the values for dN/dz estimated in this manner over-estimate the true absorption-cross section of gaseous halos because galaxy halos can overlap with each other (in particular satellite galaxies and their hosts), so that the effective halos cross section of a galaxy ensemble would be smaller than the sum of A for all individual galaxies in that ensemble. This effect is commonly investigated in studies that aim at characterizing the relationship between the stellar masses of galaxies and their superordinate dark matter (DM) halos, e.g., by using statistical methods such as the Halo Occupation Distribution (HOD) formalism and others (e.g., Peacock & Smith 2000; Moster et al. 2010). From these models follows that, on average, only the most massive halos (with DM halo masses $> 10^{11.8} M_{\odot}$, corresponding to $L > 2L^*$) are occupied by more than one galaxy. These halos are rare, however, and their contribution to dN/dz is small (see Fig. 8), so that a small change in the absorption cross section of such massive halos basically would have no influence on the estimate of the integrated number density of intervening absorbers.

A comparison between the estimated gas cross section of galaxy halos from our model with the observed number density of intervening Si III absorbers allows us to draw some very interesting conclusions. The first important conclusion is that, *because $dN/dz(\text{Si III}) < dN/dz(\text{model})$ for $\log N(\text{Si III}) > 12.2$, the entire population of these Si III systems can be explained by metal-enriched gas that is gravitationally bound to galaxies*, i.e., there is no need for an intergalactic gas component that hosts Si III absorbers at this strength. Turning this argument around, our model also predicts that intervening metal absorbers with number densities $dN/dz > 9$ (e.g., O VI absorbers with $dN/dz \approx 16$; Tripp et al. 2008) must partially arise from gas outside of the virial radius of galaxies. This aspect is further discussed in Sect. 8. A second conclusion is that for our preferred model with $\alpha = -1.1$ and $\phi^* = 0.0125 h^3 \text{ Mpc}^{-3}$ (Montero-Dorta & Prada 2009) the mean covering fraction of Si III within R_{vir} is expected to be $\langle f_c \rangle = 2.5 \pm 0.4/3.6 = 0.69 \pm 0.11$, a value that is similar to the covering fraction of Si III in the halo of the Milky Way, as recently derived from QSO absorption-line observations (Herenz et al. 2013; Lehner et al. 2012). In Sect. 6 we further investigate, whether the *observed* distribution of galaxies around Si III absorbers is in line with these conclusions.

Our model further allows us to predict the mean absorption fraction around galaxies as a function of impact parameter ρ . We here define the mean absorption fraction as the detection rate of intervening absorption from CGM gas for a given impact parameter for a population of galaxies with different virial radii. Only the most luminous galaxies with large R_{vir} are expected to contribute to the mean absorption at $\rho > 100 \text{ kpc}$, while for small impact parameters $\rho < 50 \text{ kpc}$ both luminous as well as faint galaxies do contribute. Consequently, the mean absorption fraction

around galaxies is expected to decline in a way that is determined by the distribution of R_{vir} (and thus by the shape of the galaxy luminosity function).

In Fig. 9 we show the mean absorption fraction plotted against ρ (in bins of 50 kpc), as derived from our preferred model with Schechter parameters $\alpha = -1.1$ and $\phi^* = 0.0125 h^3 \text{ Mpc}^{-3}$. As expected, the absorption rate decreases rapidly with increasing impact parameter because the fraction of sightlines that pass galaxies at $\rho > R_{\text{vir}}$ increases. Fig. 9 can be directly compared to the observed absorption rate around low-redshift galaxies, as is presented in Sect. 6.

Another important piece of information that can be extracted from our model concerns the expected covering fraction of circumgalactic gas around a population of galaxies in a given luminosity range. It is useful to transform the absorption rate into an *effective covering fraction*, $\langle \mathcal{F}_c(r_{\text{max}}) \rangle$, that is normalized to a *fixed* radius r_{max} (instead of being normalized to R_{vir} , which depends on the galaxy's mass and luminosity). To carry out this transformation we need to take into account that the covering fraction describes the detection rate per unit *area*. Since the area of each ring with thickness Δr and radius r is $\Delta r 2\pi r$, the absorption rates need to be weighted with r and integrated from $r = 0$ to $r = r_{\text{max}}$ to obtain $\langle \mathcal{F}_c(r_{\text{max}}) \rangle$. In this way, it is possible to predict from our model the effective covering fractions for different values of r_{max} for a population of galaxies in a given luminosity range. In Table 2 we list the predicted effective CGM covering fractions for different values of r_{max} , $\langle f_c \rangle$, and different luminosity ranges based on the preferred parameters for the galaxy luminosity function (see Table 1). We would like to emphasize again that in this approach $\langle \mathcal{F}_c \rangle$ describes the average CGM covering fraction of a population of galaxies within an annulus with a fixed radius, while $\langle f_c \rangle$ describes the mean covering fraction of the galaxies' CGM within R_{vir} .

6. Observed absorber-galaxy connection

6.1. Individual galaxies associated with Si III absorbers

To characterize the true absorber-galaxy connection at $z \leq 0.1$ we have calculated the geometrical impact parameters ρ between the sightlines that exhibit Si III absorbers at $z \leq 0.1$ in our COS data and nearby galaxies in our galaxy catalog (see Sect. 3.3).

Ideally, one would study the relation between absorbers and galaxies using the absorber-galaxy cross-correlation function together with a well-defined galaxy completeness function. Our galaxy sample, that is based on many different galaxy surveys and individual observations, is highly inhomogeneous with respect to the completeness limit at the faint end of the B band magnitude distribution, however, and therefore a statistically meaningful galaxy completeness function cannot be obtained. We would like to point out, however, that the motivation for including these galaxy data in our study is not to provide a statistically complete sample of absorber/galaxy pairs, but to qualitatively check the plausibility of our hypothesis, in which most Si III absorbers at $z \leq 0.1$ arise in the extended gaseous halos of luminous low-redshift galaxies, for which the present galaxy data sample is sufficient in depth.

Because of the above mentioned limitations we cannot simply combine the impact-parameter distributions of the

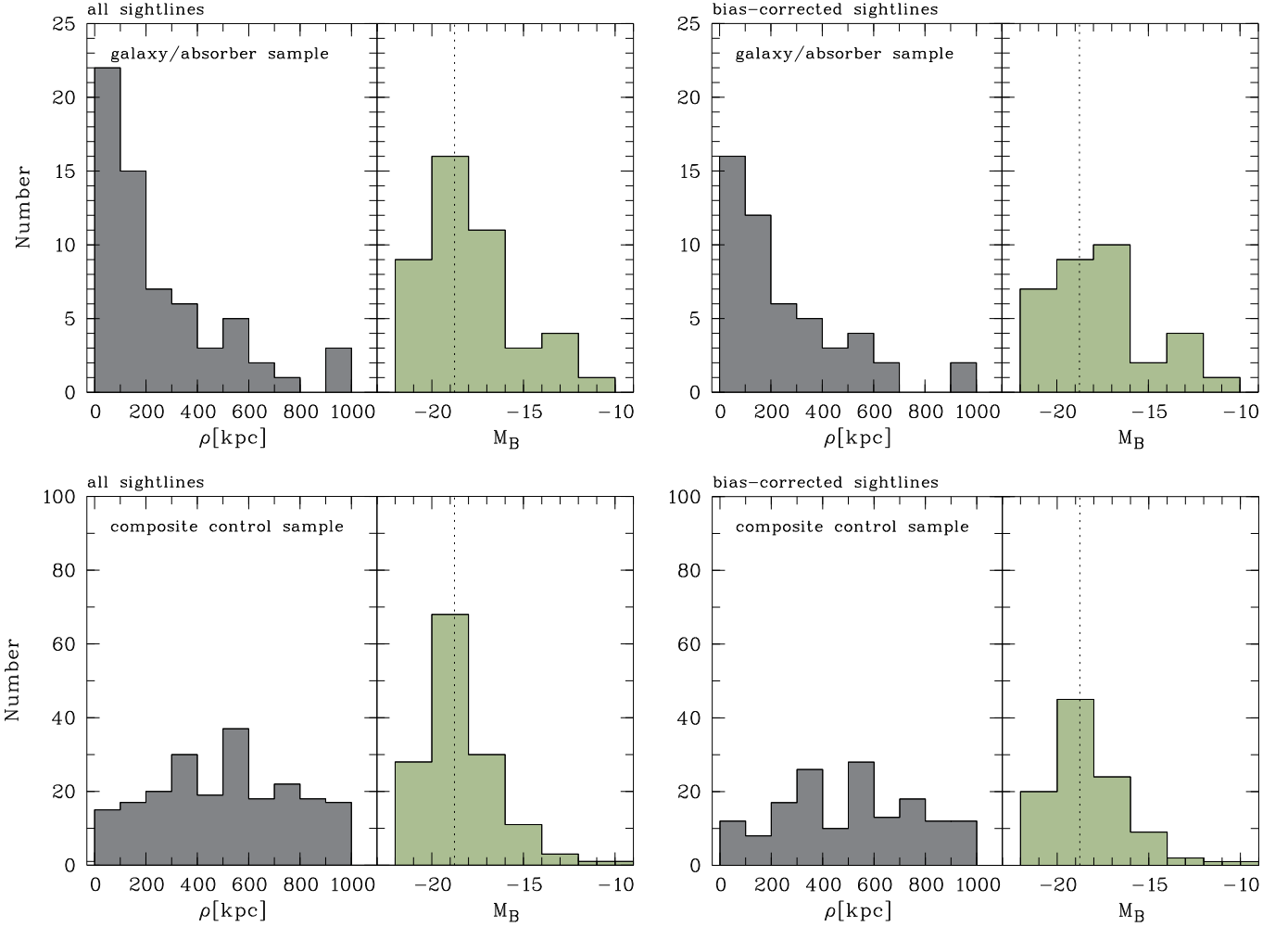


Fig. 10. *Upper panels:* Distributions of impact parameters and absolute B -band magnitudes for galaxies that are located within $|\Delta v| = 1000 \text{ km s}^{-1}$ of the absorbers (galaxy/absorber samples). On the left-hand side we show the distributions for all sightlines that exhibit Si III absorption, while on the right-hand side only the bias-corrected set of sightlines is considered (see Sect. 4.2). Galaxies tend to cluster around the LOS in velocity regions where intervening absorption is observed. *Lower panels:* The same distributions for galaxies that have no absorption systems within $|\Delta v| = 1000 \text{ km s}^{-1}$ (composite control samples; see Sect. 6.2 for details). No clustering is observed in this case.

individual sightlines to statistically investigate the overall absorber-galaxy connection, but instead have to evaluate the connection between absorbers and galaxies along each sightline *individually* before combining the results. In the following, we further specify our strategy how to do this.

For each sightline that contains an intervening Si III absorber we first selected all galaxies that have recession velocities within $|\Delta v| = 1000 \text{ km s}^{-1}$ of the absorber (hereafter referred to as “LOS absorber sample”) and identified the galaxy with the smallest impact parameter to the sightline. For the same line of sight we then created a set of nine galaxy control samples covering the adjacent velocity range $|\Delta v| = 1000 - 10,000 \text{ km s}^{-1}$, where each LOS control sample spans a velocity range of $|\Delta v| = 1000 \text{ km s}^{-1}$, similar as for the LOS absorber sample. We again marked the galaxies that are nearest to the LOS. The galaxy samples constructed in this way have the same magnitude completeness for each sightline.

If intervening absorbers would trace the CGM of galaxies that are close to the sightlines (as we suspect), one would expect for a large-enough absorber/galaxy sample (as provided here) that the impact parameters of the nearest galaxy to the LOS in the absorber samples are, on average, substantially smaller than in the control samples. Such a trend is indeed seen in our data: for 76 percent of the LOS that exhibit an intervening Si III absorber, the galaxy with the smallest impact parameter is located within 1000 km s^{-1} of the absorption redshift.

In the upper panels of Fig. 10 (gray-shaded histograms) we show the distribution of ρ for the nearest galaxies in the LOS absorber samples (“galaxy/absorber sample”) for all sightlines with Si III absorbers (left column) and for the bias-corrected set of sightlines with Si III absorbers (right column). Obviously, galaxies cluster around sightlines if an Si III absorber is present. This trend is evident in both galaxy/absorber samples (total sample and bias-corrected sample), but in the (biased) total sample there are more

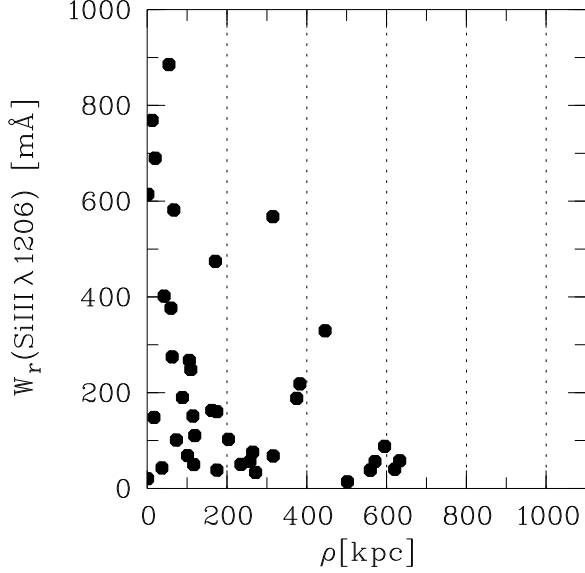


Fig. 11. Restframe equivalent widths of Si III $\lambda 1206$ are plotted against the impact parameters of the galaxies nearest to the absorbers. For increasing impact parameters the maximum value for W_r is decreasing from $W_r \approx 900$ mÅ down to values < 100 mÅ.

data points in the lowest ρ -bin, as is expected from the design of the Bordoloi et al. (2014) COS-Dwarfs survey (see Sect. 4.2).

Still, in the bias-corrected galaxy/absorber sample, 56 percent of the galaxies are located at impact parameters $\rho < 200$ kpc and for the same percentage the velocity difference between the galaxy and the absorber is $|\Delta v| \leq 300$ km s $^{-1}$. From our model we would expect that the maximum impact parameter in an idealized galaxy sample is $\rho \approx 300$ kpc, as this length scale corresponds to the virial radius of the most luminous galaxies that are expected to significantly contribute to the number density of Si III absorbers before the galaxy-density distribution breaks down for higher luminosities (Fig. 8, middle panel). However, since our galaxy sample is incomplete and highly inhomogeneous along the different LOS with respect to galaxies at the faint end of the luminosity function, the observed distribution of ρ extends much further out. With the green-shaded histogram we show in Fig. 10 the absolute B -band magnitudes for the galaxies in the galaxy/absorber samples, as calculated from their cosmological distance. The dotted line indicates the absolute B magnitude of an L^* galaxy (adopted from Montero-Dorta & Prada 2009).

To check the statistical significance of this clustering trend we analyzed the galaxies in the respective control samples in a similar manner. We find that the galaxies do not cluster around the sightlines in any of the control samples, but their impact parameters are more or less evenly distributed. To demonstrate this, we show in the lower left and right panels of Fig. 10 the impact-parameter distributions in the control samples, i.e., for galaxies that have no absorption systems within $|\Delta v| = 1000$ km s $^{-1}$. For this, we combined for each of the two data sets (total sample/bias-corrected sample) the nine individual control samples to one “composite control sample”, respec-

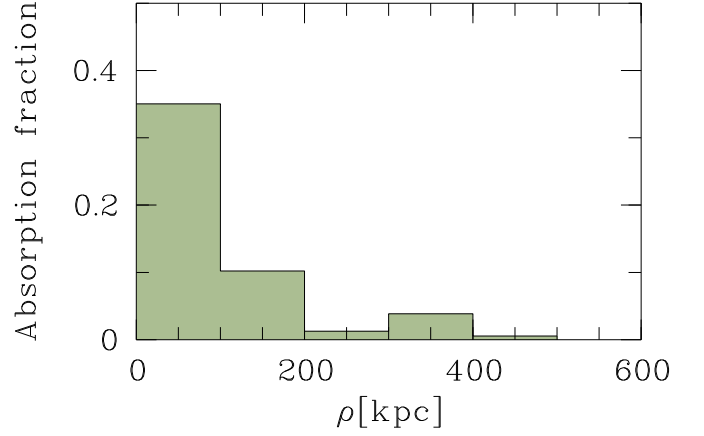


Fig. 12. Absorption fraction (fractional abundance of intervening absorbers per galaxy) as a function of impact parameter, as measured in our galaxy/absorber sample.

tively, which contains all galaxies within the velocity window $|\Delta v| = 1000 - 10,000$ km s $^{-1}$ with respect to the absorber redshift (see above).

The distributions of absolute B -band magnitudes in the composite control samples (Fig. 10, lower left panel, green-shaded areas) are similar to those in the galaxy/absorber samples, proving that the different galaxy samples have the same completeness in B .

In summary, the observed absorber-galaxy relation strongly suggests that the galaxies “know” about the presence of nearby Si III absorption systems. This is exactly what would be expected if the absorption were (predominantly) caused by metal-enriched gas in the extended halos and the superordinate cosmological environment of these galaxies.

For our bias-corrected galaxy/absorber sample we calculate effective covering fractions of $\langle \mathcal{F}_c(r_{\max}) \rangle = 0.08$ for $r_{\max} = 400$ kpc and $\langle \mathcal{F}_c(r_{\max}) \rangle = 0.01$ for $r_{\max} = 1000$ kpc. These effective covering fractions are comparable to those expected for a population of $L > 0.1L^*$ galaxies that are surrounded by a CGM that reaches out to R_{vir} with $\langle f_c \rangle = 0.75$ (Table 2).

6.2. Absorption strength vs. impact parameter

In Fig. 11 we plot the restframe equivalent widths of Si III $\lambda 1206$ versus the impact parameters of the galaxies nearest to the absorbers. For $\rho < 200$ kpc the equivalent width scatters strongly in the range 10 – 1000 mÅ. For increasing impact parameters the maximum value for W_r (hereafter referred to as $W_{r,\max}$) is decreasing to values < 100 mÅ for $\rho > 600$ kpc.

The interpretation of this plot is not as simple as it may look like: because of the incompleteness of the galaxy sample, the largest values for ρ (which are far beyond the virial radii of the most massive galaxies) do not represent true impact parameters to the nearest galaxies, but rather indicate the impact parameters to the nearest *luminous* galaxies. From observations of strong Mg II absorbers it is known that the mean Mg II $\lambda 2796$ equivalent width in the CGM of luminous galaxies is larger than for low-luminosity galaxies (e.g., Nielsen et al. 2013). Assuming that a similar trend holds for Si III, the large scatter for $W_r(\text{Si III } \lambda 1206)$

at $\rho < 200$ kpc can be interpreted by the large range in luminosities of the galaxies whose circumgalactic gas causes the absorption, where $W_{r,\max}$ is determined by the most luminous galaxies. The decline of $W_{r,\max}$ for increasing ρ then simply reflects the decreasing likelihood to *miss* luminous galaxies around the absorbers that are responsible for the strongest absorbers. For large values of ρ , only absorbers with small W_r values remain, as they belong to low-luminosity galaxies that are too faint to be covered in our galaxy sample.

6.3. QSO sightlines associated with individual galaxies

We now investigate the absorber/galaxy-connection from the perspective of the galaxies. For each galaxy in our sample we first identified QSO sightlines that pass the galaxies at impact parameters $\rho < 1000$ kpc. We then further selected only galaxies in redshift ranges that are covered by each relevant COS spectrum at a S/N that is high enough to detect Si III absorption at column densities $\log N_{\text{lim}}(\text{Si III}) \geq 12.2$. Finally, we calculated for each 100 kpc wide impact-parameter bin the absorption fraction (i.e., the fraction of galaxies having a Si III absorber above this column density limit in this impact-parameter range). The result from this analysis is shown in Fig. 12. As can be seen, the observed absorption fraction is substantially smaller than the one derived from the idealized halo model (Fig. 9), but extends to much larger impact parameters even beyond the expected virial radii of massive galaxies. We again interpret this behavior as a sign for the incompleteness in our galaxy data, i.e., we suspect that sightlines that have apparent galaxy impact parameters in the range $300 \leq \rho < 1000$ kpc are arising from halo gas within the virial radii of *unseen* galaxies.

7. Ionization conditions

7.1. Model setup

To gain insight into the physical properties of the intervening Si III absorbers and to estimate the total gas mass that they trace we studied the ionization conditions in the absorbers using the ionization code Cloudy (v13.03; Ferland et al. 2013). The absorbers are modelled as plane-parallel slabs with fixed neutral gas column densities; they are exposed to the UV background radiation with $\log \Gamma = -13.6$ (see Sect. 2 for more details on the used UV background field) and are assumed to be optically thin in H I.

In Sect. 4 we have suggested that Si III traces at least two characteristic gas phases, a more ionized, diffuse phase that is also traced by Si IV, and a more dense (partly neutral) phase that is also detected in Si II. For our Cloudy modeling we therefore have focused on the relation between the column densities of H I, Si II, Si III, and Si IV as a function of the ionization parameter U , the ratio between ionizing photon density and total particle density (i.e., $U = n_\gamma/n_H$). For an assumed ionizing radiation field one can calculate n_γ and thus can relate U with the gas density n_H .

In Fig. 13 we have plotted (as an example) the expected H II, Si II, Si III, and Si IV column densities against $\log n_H$ for a (typical) H I column density of $\log N(\text{H I}) = 15$, based on a set of Cloudy models assuming solar abundances of all heavy elements (Asplund et al. 2009). We also show the expected trend for Mg II, which follows Si II very closely

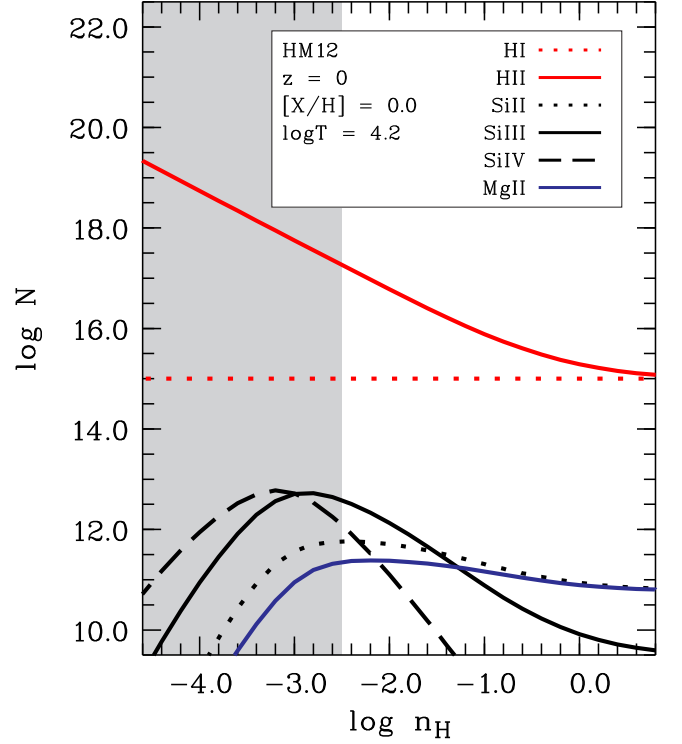


Fig. 13. Predictions of H II, Si II, Si III, Si IV, and Mg II column densities as a function of the gas density ($\log n_H$) for an H I column density of $\log N(\text{H I}) = 15$, based on a Cloudy ionization model using the local UV background and assuming absolute and relative solar abundances of all elements. The gray-shaded area indicates the density that is typical for the Si III/Si IV phase (see Sect. 7.3).

over the entire density range. This similarity justifies our previous approach to estimate the number density of strong Mg II using Si II as a proxy (Sect. 4.3.2). We have set up a grid of Cloudy models in which we have varied the H I column density in the range $\log N(\text{H I}) = 14 - 19$ to provide column-density predictions for the above listed ions.

The most important conclusion from this modeling is that the shapes of the column-density curves for H II, Si II, Si III, Si IV, and Mg II (and their positions relative to each other) basically do not depend on $\log N(\text{H I})$, implying that the observed column density ratios of the Si ions can be used to constrain n_H in optically thin H I/Si III absorbers even without knowing $N(\text{H I})$.

Fig. 13 further indicates that Si IV becomes the dominant ion of Si only for relatively low gas densities ($\log n_H < -3.5$), while Si III dominates in the density range $-3.5 < \log n_H \leq -2.0$. Si II is dominant at $\log n_H > -2.0$, thus at densities that are expected to be relevant only for DLAs and sub-DLAs in the neutral gas disks and in predominantly neutral gas structures in the inner halos of galaxies (e.g. in high-velocity clouds).

7.2. Single-phase model

One may assume that the simultaneous absorption of Si II, Si III, and Si IV at similar radial velocities, such as observed in some systems, stems from a single gas phase in the absorbers. For that case, our Cloudy models provide some

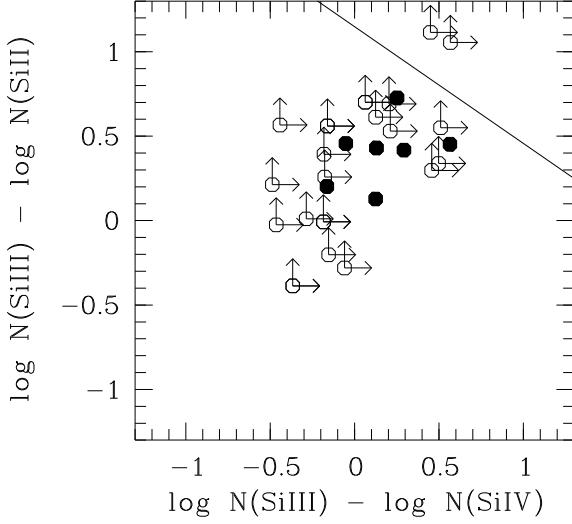


Fig. 14. Column-density ratios of Si III/Si II vs. Si III/Si IV are plotted together with predictions from the single-phase Cloudy model (equation 5, indicated by the black solid line). Measured values are plotted with filled circles, limits are indicated with open circles. For none of the systems do the data points lie on the expected relation for the single-phase model, implying that the gas is multiphase.

firm predictions for the allowed column-density ranges for these three ions that can be summarized by the following parametrization of the expected column-density ratios Si III/Si IV and Si III/Si II in a single gas phase:

$$\log \left[\frac{N(\text{Si III})}{N(\text{Si IV})} \right] = 1.68 - 1.44 \log \left[\frac{N(\text{Si III})}{N(\text{Si II})} \right]. \quad (5)$$

In Fig. 14 we have plotted the observed column-density ratios of these ions (and relevant limits) together with predictions from the Cloudy model as given in equation (5) (the model is indicated in Fig. 14 by the black solid line). For none of the systems that have measured column densities for Si II, Si III, and Si IV (Fig. 14 filled circles) do the data points lie on the expected relation for the single-phase model. For all systems for which we have measured values in these three ions the Si II and/or Si IV column densities are too high for the observed Si III column density to match the single-phase model. While we cannot exclude that at least some of the systems for which only lower limits for Si III/Si IV and Si III/Si II are available are in accordance with the single-phase model, the observations clearly do not favor such a scenario, but rather point towards a more complex multiphase nature of gas, as considered below.

7.3. Multi-phase model

The alternative (and probably more realistic) model for the absorbers is that of a multiphase gas, where Si II and Si IV predominantly trace different gas phases (and different physical regions) that coexist within the same overall absorbing gas structures. In the Milky Way halo, the existence of multiphase halo gas as traced by various low, intermediate, and high ions is well established (e.g., Sembach et

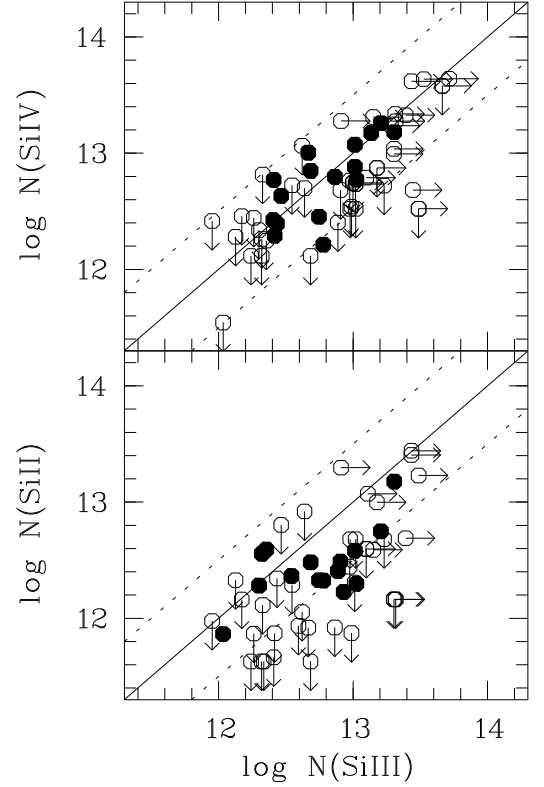


Fig. 15. Distribution of logarithmic column densities in the Si III absorbers. *Upper panel:* Si IV vs. Si III (absolute values indicated with filled circles, limits with open circles). *Lower panel:* Si II vs. Si III. The dotted/solid lines indicate ratios of +0.5, 0, -0.5 dex, respectively.

al. 2003; Fox et al. 2006; Collins et al. 2009; Shull et al. 2009; Richter et al. 2009; Herenz et al. 2013).

For the following we assume that Si III absorption arises in both a diffuse ionized gas phase traced by Si IV/Si III as well as a somewhat denser (partly neutral) gas phase traced by Si II/Si III. To further investigate the characteristic densities of these two phases we have plotted in Fig. 15 the column densities $\log N(\text{Si III})$ vs. $\log N(\text{Si IV})$ (upper panel) and $\log N(\text{Si III})$ vs. $\log N(\text{Si II})$ (lower panel). Data points from measured column density limits in these ions are plotted with open circles. Because both gas phases defined above may be present in an absorber, the plotted values of $\log N(\text{Si III})$ have to be regarded as an upper limit for the Si III column in each phase.

For the absorbers that are detected simultaneously in Si III and Si IV (upper panel of Fig. 15, filled circles) the data points scatter within ~ 0.7 dex around the $N(\text{Si III}) = N(\text{Si IV})$ line. For the absorbers that are detected simultaneously in Si III and Si II (lower panel of Fig. 15, filled circles) the measured Si II column densities are typically lower than that of Si III, but (again) note that a considerable fraction of the Si III column may arise in the Si IV phase, so that $\log [N(\text{Si II})/N(\text{Si III})]$ could be much higher locally.

Because of the unknown intrinsic structure of each absorber it is challenging to provide firm predictions for the gas density for each individual system that has measured Si II/Si III/Si IV column densities. From the exploration of the parameter space the Cloudy models deliver, however, a

characteristic gas density that separates the Si IV/Si III from the Si II/Si III phase in the absorbers (see also Fig. 13). We find that the Si IV/Si III phase traces gas with densities $\log n_{\text{H}} \leq -3.0$ (in Fig. 13 indicated with the gray-shaded area), while the Si II/Si III phase has higher densities in the range $n_{\text{H}} > -3.0$.

7.4. Total gas mass and baryon budget

Our observations and Cloudy models imply that Si III traces diffuse (predominantly ionized) gas in the extended gaseous halos (i.e., in the circumgalactic medium) of galaxies. An interesting question is, how much mass is contained in such gas and what is the overall baryon budget of intervening Si III absorbers and the metal-enriched CGM. To derive the total gas mass of the Si III systems in our sample we need to calculate the amount of ionized hydrogen in each absorber. Because of the much higher ionization fraction in the Si IV/Si III systems compared to the Si II/Si III phase we here concentrate on the estimate of $N(\text{H II})$ in low-density Si III absorbers that are associated with Si IV.

For the range $\log N(\text{H I}) = 14 - 17$ our Cloudy model grids imply a relatively simple relation between the minimum H II column density and the Si III column density in each absorber:

$$\log N(\text{H II}) \approx \log N(\text{Si III}) + \log Y - \log (\text{Si}/\text{H})_{\odot}, \quad (6)$$

where the parameter Y , that solely depends on the gas density, needs to be determined from the observed Si IV/Si III ion ratios (Fig. 13). Since we do not know what fraction of the Si III column density can be assigned to the Si IV phase, we can only place a lower limit to Y (see above). Similarly, because of the unknown metallicity of the CGM, we have to assume an upper limit for the silicon abundance (Si/H) in the gas. Equation (6) allows us to derive a lower limit for $N(\text{H II})$ in each Si IV/Si III absorber, from which the integrated (=total) column density, $N(\text{H II})_{\text{tot}}$, can then be determined.

The cosmological mass density of the Si IV/Si III absorbers in terms of the current critical density, ρ_c , can be estimated by

$$\Omega_b(\text{Si III}) \equiv \frac{\mu m_{\text{H}} H_0}{\rho_c c} N(\text{H II})_{\text{tot}} \Delta X_{\text{tot}}^{-1}, \quad (7)$$

with $\mu = 1.3$, $m_{\text{H}} = 1.673 \times 10^{-27}$ kg, $H_0 = 69.7$ km s⁻¹ Mpc⁻¹ (Hinshaw et al. 2013), and $\rho_c = 3H_0^2/8\pi G$. The comoving path length ΔX available for the detection of Si IV/Si III absorbers along each sightline is given by:

$$\Delta X \equiv (1+z)^2 [\Omega_m(1+z)^2 + \Omega_{\Lambda}]^{-1/2} \Delta z_{\text{abs}}. \quad (8)$$

The integration over all sightlines then delivers ΔX_{tot} . For our bias-corrected Si IV/Si III absorber sample with $\log N(\text{Si III}) \geq 12.2$ we have $N(\text{H II})_{\text{tot}} \geq 5.4 \times 10^{20}$ cm⁻² and $\Delta_{\text{tot}} X = 20.65$. The cosmological mass density can then be written as $\Omega_b(\text{Si III}) \geq 4.6 \times 10^{-4} Z_{\text{Si}}$, where Z_{Si} is the Si abundance in the gas relative to the solar value, $\log (\text{Si}/\text{H})_{\odot} = -4.49$ (Asplund et al. 2009). Thus, if the CGM traced by Si III would have a solar Si abundance, it would contain roughly as much mass as the neutral ISM within galaxies at $z = 0$ ($\Omega_b(\text{H I}) = 4.7 \pm 0.7 \times 10^{-4}$; Zwaan et al. 2005).

On the one hand, $\Omega_b(\text{Si III})$ could be much higher, if the mean metallicity of the gas was substantially lower than solar. This appears plausible if most of the gas originates in the IGM, e.g., as material stemming from accretion flows. Lehner et al. (2013) studied the metallicity distribution of LLS at $z \leq 1$ and found two distinct populations of absorbers with mean metallicities of 0.03 solar (population I) and 0.50 solar (population II). They suggest that population I absorbers represent metal-poor circumgalactic gas from accretion streams, while population II systems trace metal-enriched halo material from galaxy outflows and winds. In view of these results, we assume a value of $Z_{\text{Si}} = 0.5$ as a conservative upper limit for the metallicity of the Si III absorbers in our survey. This value leads to $\Omega_b(\text{Si III}) \geq 9.2 \times 10^{-4}$, roughly twice the value of the neutral ISM within galaxies.

Earlier theoretical and observational studies that addressed the outflow of gaseous material from galaxies and the enrichment of the IGM suggested, on the other hand, that the metals produced within galaxies escape in the form of metal-rich (super-solar, eventually) gas pockets (Mac Low & Ferrara 1999; Rauch et al. 2001; Schaye, Carswell & Kim 2007). Such gas pockets could mimic the absorption properties of intervening metal absorbers, but they would carry only very little mass. While it cannot be excluded that some of the Si III absorbers presented in this study belong to such metal patches with above-solar metallicities, the large overall cross section of circumgalactic Si III together with the expected cosmological metal-mass density at $z = 0$ (e.g., Calura & Mateucci 2004) excludes that a dominating fraction of the circumgalactic Si III absorbers have metallicities above solar.

From the above considerations we conclude that the Si IV/Si III bearing gas phase in the CGM of low redshift galaxies contains (possibly substantially) more baryonic matter than their neutral ISM. This conclusion is supported by previous estimates of the baryon content of the cool, photoionized CGM in the local Universe from the COS-Halos survey (Werk et al. 2014).

8. Discussion

8.1. On the origin of intervening Si III absorbers

Our study indicates a tight spatial correlation between intervening Si III absorbers at $z \leq 0.1$ and the local galaxy population at impact parameters ≤ 400 kpc, suggesting that the majority of these absorption systems arise in the extended gaseous halos of these galaxies. This interpretation is supported by recent *HST*/STIS and *HST*/COS observations of Si III absorption in the CGM of the Milky Way (Shull et al. 2009; Collins et al. 2009; Richter et al. 2009; Lehner et al. 2012; Herenz et al. 2013; Richter et al. 2016, in prep.), who show that doubly-ionized Si has the largest absorption cross section of all low, intermediate and high ions with a sky covering fraction of $\langle f_c \rangle \approx 0.7$. While the distances and the space distribution of Si III absorbers in the Milky Way halo still are unclear (owing to our internal vantage point), Lehner et al. (2015) demonstrated that M31 also exhibits an extended, metal-enriched gaseous halo that gives rise to Si III absorption out to ~ 200 kpc. Finally, other groups that have studied the absorption properties of the CGM for individual galaxies (e.g., Keeney et al. 2013), or pre-selected galaxy samples such as the COS-Halos sur-

vey (e.g., Tumlinson et al. 2011, 2013; Werk et al. 2013; Peebles et al. 2013) demonstrate that Si III is ubiquitous in the extended CGM of low-redshift galaxies. The existence of such discrete Si III bearing gas complexes with temperatures $T < 10^5$ K (thus below the virial temperature of their DM host halos) in the extended circumgalactic environment of galaxies can be understood in terms of the steady circulation of hot and cold gas through the CGM ("circumgalactic fountain") as part of the ongoing galaxy evolution. In this scenario, star formation in galaxies drives out large amounts of (hot) metal-enriched gas. Even if this material leaves the potential well of an individual galaxy, it is trapped by the superordinate cosmological structure. From there, the gas may (slowly) fall back onto the galaxy of its origin in the form of discrete gas structures, as the gas never reaches hydrostatic equilibrium during such a circulation cycle (Ford et al. 2014). Alternatively, the gas may be accreted by a *different* galaxy nearby, or heated up to the virial temperature of the superordinate DM halo, in which case it may remain extragalactic forever.

While the observed frequency of Si III absorbers with $\log N(\text{Si III}) \geq 12.2$ and the derived impact parameter distribution are in line with a scenario, in which *all* Si III absorbers are located within the virial radius of intervening galaxies and thus are gravitationally bound to them, it cannot be excluded that there exists a population of intervening Si III absorbers that traces gas at larger distances. This is actually expected, since in many cases large, gas-rich spiral galaxies like the Milky Way do not represent isolated systems, but are part of a galaxy group, which binds metal-enriched diffuse gas within its own virial radius in the form of an intragroup medium.

Stocke et al. (2014) recently have studied a class of "warm" H I/O VI absorbers using COS spectra. They suggested that these systems trace an extended (Mpc scale) $T = 10^5 - 10^6$ K intragroup medium in spiral-rich galaxy groups. If such warm gas was typical for group environments, it appears plausible that one would find cooler ($T < 10^5$ K) gas patches embedded in such a medium that could give rise to intervening Si III/Si IV absorption. Some of the galaxy/absorber pairs that have apparent impact parameters in the range $\rho = 200 - 1000$ kpc may belong to such group absorbers. The Cloudy modeling predicts that Si III/Si IV absorbers trace gas down to thermal pressures of $P/k = n_{\text{H}}T \sim 1 \text{ cm}^{-3} \text{ K}$. For gas that is gravitationally bound to individual galaxies, such low gas pressures would be expected only in the outermost regions of galaxies near their virial radius (see also discussion in Shull 2014). However, such a value for P/k also would be in agreement with the expected range of gas pressures in galaxy groups (Stocke et al. 2013).

Our survey suggests that the number density distribution of Si III absorbers breaks down for column densities $\log N(\text{Si III}) \leq 12.2$ (Fig. 4, right panel), which is not a completeness effect in our data (see Sect. 4.1). These low-column density systems may represent the prime candidates for metal-enriched cloudlets that arise in regions with low gas densities (and pressures), such as in group environments and in the IGM. As pointed out by Stocke et al. (2013), the expected number density of galaxy groups is ten times less than the space density of L^* galaxies (Berlind et al. 2006). Interestingly, the number density of Si III absorbers with $\log N(\text{Si III}) \leq 12.2$ is also ~ 10 times less than the number density of absorbers with $\log N(\text{Si III}) \geq 12.2$, supporting a

scenario in which high-column density Si III systems trace the CGM of galaxies, while low-column density Si III systems arise in the intragroup gas of galaxy groups.

With the occurrence of several galaxies at impact parameters $\rho < 1000$ kpc to the QSO sightlines and with radial velocities close to the observed absorber velocities (such as expected for group environments), the interpretation of the observed absorption with respect to origin and nature of the gas in its galaxy environment generally is tricky. While a more systematic investigation between intervening Si III absorbers and galaxy group environments clearly is beyond the scope of this paper, we show in Fig. 16 as a prominent example the galaxy group environment of the $z = 0.0037$ Si III absorber towards the QSO 1H0419–577 (IRAS F04250–5718). This sightline passes two galaxies in the Dorado galaxy group (Kilborn et al. 2005; Maia, Da Costa & Latham 1989) at impact parameters $\rho < 220$ kpc. In principle, the observed Si III absorption at $cz = 1109 \text{ km s}^{-1}$ could be associated with either of these two galaxies, which have radial velocities of $v_r = 1050$ and 1215 km s^{-1} (Kilborn et al. 2005). The observed gas may be infalling or outflowing gaseous material; the metallicity of the absorber lies in the range between 0.1 – 1.0 solar (as derived from the fit of the H I Ly α absorption together with the Cloudy model of the Si III/Si IV absorption), thus in line with both scenarios. However, the absorber could also be located outside the virial radii of these two galaxies and may belong to a faint (unseen) dwarf galaxy in the same group or may represent a metal-rich gas patch embedded in the intragroup medium of the Dorado group. The interpretation of *individual* absorber/galaxy pairs thus remains inconclusive with magnitude-limited galaxy data. The statistical connection between galaxies and intervening Si III systems, as studied here, yet demonstrates that both class of objects trace the same Mpc-scale environment within the cosmic web.

8.2. Comparison with previous Si III absorption-line studies

We are not aware of any other systematic studies in the literature that focus explicitly on Si III-selected intervening absorption systems and their relation to galaxies. There are, however, several absorption-line surveys at low redshift (using various UV spectrographs) that provide information on the number density of Si III and other intermediate ions (e.g., C III) and the distribution of equivalent widths/column densities of these ions.

Tilton et al. (2012) compiled UV absorption-line data from *HST*/STIS and *FUSE* and prepared a catalog of UV absorbers for redshifts $z < 0.4$. From their data sample they derive a number density of intervening Si III absorbers of $dN/dz = 7.4^{+2.1}_{-1.2}$ for $\log N(\text{Si III}) > 12.2$ for this redshift range, based on a total redshift path of $\Delta z \approx 5.2$. This value is more than twice the value derived in this study. The same authors recently published another absorption-line catalog of intervening absorption systems at $z < 0.4$, this time based on *HST*/COS data of 75 QSOs (Danforth et al. 2016). In this new survey, the authors derive a number density of $dN/dz \approx 7$ for $\log N(\text{Si III}) > 12.2$ and $z < 0.1$. Moreover, their study suggests an *increase* for $dN/dz(\text{Si III})$ for decreasing redshift in the local Universe (their Fig. 15). Their new value again is substantially higher than the value derived by us. To investigate the origin for this discrepancy we have carefully compared their absorber list with ours,

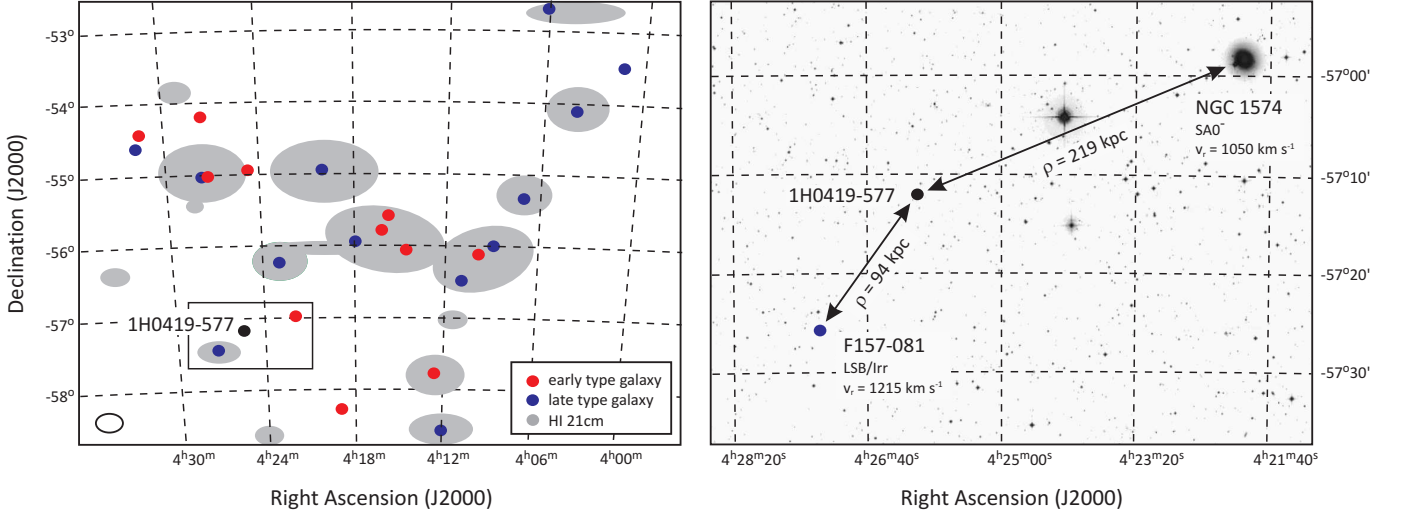


Fig. 16. *Left panel:* Distribution of galaxies and H I in the Dorado galaxy group (see Kilborn et al. 2005 and references therein). Intervening Si III absorption is observed at $z = 0.0037$ ($cz = 1109 \text{ km s}^{-1}$) towards the QSO 1H0419–577 (black filled circle). The absorption most likely is associated with the CGM of one group member or with the intergroup medium. *Right panel:* Zoom-in for the region around the two group members F157–081 and NGC 1574; the absorber could be associated with either or both of these galaxies given its velocity and projected distance to each of the systems.

as our COS data sample includes all of the 75 QSOs presented in Danforth et al. (2016). We suspect that the higher value for $dN/dz(\text{Si III})$ derived by Danforth et al. (2016) stems from the less stringent selection criteria for identifying metal absorbers and defining the relevant absorption path lengths along their sightlines. Also, a possibly existing selection bias in their QSO sample may be the reason for the higher value of $dN/dz(\text{Si III})$.

We identify three Si III systems in their absorber list, whose identifications are based on absorption features that (in our opinion) most likely have different origins. We also have identified one candidate Si III absorber that is not listed in the Danforth et al. (2016) paper. In Table A.12 in the Appendix we list these discrepant absorption systems together with a short description of the absorption characteristics.

As we discuss in one of the following sections, state-of-the-art hydrodynamical simulations of metal-enriched gas in the local Universe do not support values of $dN/dz > 5$ for Si III absorbers for $\log N(\text{Si III}) > 12.2$, but favour Si III number densities of < 4 for $z \approx 0$.

8.3. Comparison with other CGM studies

As mentioned above, Si III is frequently detected in the CGM of individual galaxies (Keeney et al. 2013; Lehner et al. 2015) and in the CGM of pre-selected galaxy samples (e.g., COS-Halos; Tumlinson et al. 2013; Werk et al. 2013; Liang & Chen 2014). Our study, which represents a statistical rather than a targeted study of the CGM in the local Universe, complements most of the previous observational CGM studies. Many of the COS sightlines that have been used by previous, targeted CGM studies are included in our sample. Because of the statistical nature of our survey, we refrain from comparing our results for *individual* galaxy/absorber pairs with results from other studies.

From an archival study of CGM absorption around 195 galaxies at $z < 0.176$ Liang & Chen (2014) find a mean

Si III covering fraction of $0.60^{+0.13}_{-0.18}$ within $0.54 R_{\text{halo}}$ and $0.14^{+0.11}_{-0.05}$ for the range $0.54 - 1.02 R_{\text{halo}}$, but no significant Si III absorption beyond. These covering fractions are lower than our estimate of $\langle f_c \rangle = 0.69 \pm 0.11$. This is not surprising, however, since their study considers only strong Si III systems with $W_r > 100 \text{ mÅ}$ ($\log N(\text{Si III}) > 12.6$), while our estimate is based on a more sensitive search including weak and strong absorbers with $\log N(\text{Si III}) > 12.2$. If we adopt our measured value of $dN/dz(\text{Si III}) = 1.9$ for $N(\text{Si III}) \geq 12.6$ for our estimate of $\langle f_c \rangle$ using equation (4), we obtain a value of $0.47^{+0.09}_{-0.08}$ within R_{vir} , thus in good agreement with the Liang & Chen (2014) estimate. Also Werk et al. (2013) consider only strong Si III absorbers around $L \approx L^*$ absorbers with $W_r > 100 \text{ mÅ}$ and find $\langle f_c \rangle = 0.72^{+0.07}_{-0.17}$ for their total galaxy with little dependence on the galaxy mass or star-formation rate (their Table 6). Within the given error bars, these estimates for $\langle f_c \rangle$ (based on different methods) agree very well with each other.

In contrast, Bordoloi et al. (2014) studied the CGM around *dwarf* galaxies at $z < 0.1$ and found no metal absorption beyond $0.5 R_{\text{vir}}$. Their study suggests that the filling factor of warm circumgalactic gas is substantially smaller for dwarfs than for L^* galaxies. As described in Sect. 4.2, our full data set includes most of the sightlines from the Bordoloi et al. sample, so that we can analyze the Si III absorption fraction in the CGM of these dwarf galaxies directly. We find that only 17 out of the according 40 sightlines show detectable Si III with $\log N(\text{Si III}) > 12.2$ at the redshifts of the dwarf galaxies ($\langle f_c \rangle = 0.43^{+0.10}_{-0.11}$), demonstrating that the absorption fraction of the warm CGM traced by Si III around dwarf galaxies is only ~ 60 percent of that seen in galaxies with higher luminosities. The small CGM absorption fraction around dwarf galaxies is the reason for the almost identical number densities of intervening Si III in our original data sample and in the bias-corrected sample (Sect. 2.4).

Turning to high-ionization species, Wakker & Savage (2009) have studied the relation between O VI and nearby galaxies at $z < 0.017$ based on UV and FUV data along 76 extragalactic sightlines, demonstrating that a substantial fraction of the O VI systems arise from gas within R_{vir} of these galaxies (see also Prochaska et al. 2011; Tumlinson et al. 2011; Stocke et al. 2013). However, in contrast to Si III, O VI is also present beyond the virial radius of these galaxies, tracing hot metal-enriched gas (at higher gas temperatures and lower densities than Si III) that presumably has been ejected by galactic winds and outflows in past epochs of active star formation. In fact, in view of our CGM modeling results presented in Sect. 5, the measured O VI number density at low redshifts of $dN/dz(\text{O VI}) \approx 16$ (Tripp et al. 2008) indicates a very large absorption cross section of O VI that is clearly beyond the expected cross section of the CGM in the local Universe, even if non-standard Schechter parameters in the luminosity function are considered (Table 1, fourth row). The Milky Way possibly also contains a massive, extended O VI envelope that reaches deep into the Local Group potential well (Sembach et al. 2003 and Wakker et al. 2003).

Interestingly, the detailed analysis of the COS-Halos sample suggests that the absorption properties of low and intermediate ions (such as Si III) in star-forming galaxies does not significantly differ from those in passive galaxies, while O VI predominantly arises in the halo of active galaxies (Thom et al. 2012; Werk et al. 2013; Tumlinson et al. 2011). From their study, Liang & Chen (2014) conclude that the CGM becomes progressively more ionized from small to large radii. A similar conclusion was drawn by us from modeling the radial decline of the neutral gas fraction in the CGM in the Local Group (Richter 2012).

8.4. Comparison with hydrodynamical simulations

Cosmological, hydrodynamical simulations have recently become a powerful tool for studying intergalactic and circumgalactic gas at low and high redshifts (e.g., Oppenheimer & Davé 2006; Crain et al. 2013; Nuza et al. 2014). The line statistics from synthetic absorption spectra generated from such simulations can be directly compared to QSO absorption-line studies to investigate the different gas phases in the IGM and CGM and their redshift evolution (Fang & Bryan 2001; Richter et al. 2006; Fangano, Ferrara & Richter 2007; Tepper-García et al. 2011, 2012, 2013; Oppenheimer et al. 2012; Smith et al. 2011; Churchill et al. 2015).

While most of these studies have focused on the properties of high-ion absorbers, such as O VI and Ne VIII, to study the shock-heated warm-hot intergalactic medium or shock-heated gas in the CGM, intermediate ions such as Si III and C III so far have not been considered for a detailed comparison study of absorption-line statistics in simulations and observational data. From the simulations of Smith et al. (2011), Danforth et al. (2016) extracted the cumulative line density of intervening metal absorbers for a comparison with their COS absorption-line survey. While their own value for $dN/dz(\text{Si III})$ of ~ 7 for $\log N(\text{Si III}) > 12.2$ (see Sect. 8.2) lies far above the value predicted by Smith et al. for this column-density limit ($dN/dz(\text{Si III}) \approx 3$), the Si III number density derived by us is in very good agreement with the results by Smith et al.

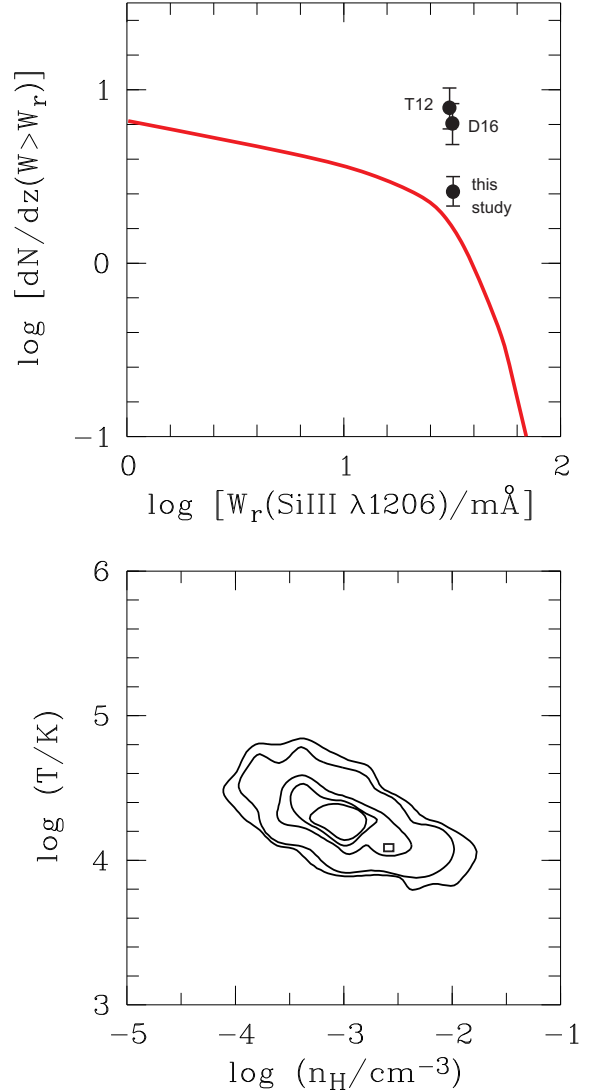


Fig. 17. *Upper panel:* Cumulative number density of intervening Si III absorbers for different equivalent-width limits predicted by a simulation run from the Overwhelmingly Large Simulations (OWLS; Schaye et al. 2010), as presented in Tepper-García et al. (2012). The measured value from this study and from Tilton et al. (2012; T12) and Danforth et al. (2016; D16) are indicated with filled circles. *Lower panel:* Phase diagram of intervening Si III absorbers in the temperature-density plane, as predicted by OWLS.

We here re-use synthetic spectra generated along random LOS from a simulation run (Model AGN) of the Overwhelmingly Large Simulations (OWLS; Schaye et al. 2010) to further investigate the frequency and physical conditions in Si III absorbers at low redshift ($z = 0.25$). Similar simulations have been used by us previously to study absorption signatures of warm-hot gas in the local Universe (Tepper-García et al. 2011, 2012, 2013). The OWLS simulations were set up using the smoothed particle hydrodynamics (SPH) code GADGET III (a modified version of GADGET II; Springel 2005) and were carried in a cubic box of $100 h^{-1}$ comoving Mpc on a side, containing 5123 dark matter (DM) and 5123 baryonic particles. The initial mass resolution is $4.1 \times 10^8 h^{-1} M_{\odot}$ (DM)

and $8.7 \times 10^8 h^{-1} M_{\odot}$ (baryonic), while the gravitational softening is set to $8 h^{-1}$ comoving kpc and is fixed at $2 h^{-1}$ proper kpc below $z = 3$. The cosmological simulations from the OWLS project are characterized by a particularly careful implementation of important physical processes that have been largely ignored in earlier studies (e.g., the influence of the photoionization on the cooling function of the gas). Details on the sub-grid physics used in OWLS can be found in Wiersma et al. (2009a; radiative cooling), Schaye & Dalla Vecchia (2008; star formation), Dalla Vecchia & Schaye (2008; stellar feedback), and Booth & Schaye (2009; AGN feedback). The strategy, how the synthetic absorption-line spectra from OWLS were set up and analyzed is presented in Tepper-García et al. (2011, 2012, 2013). In Fig. 17, upper panel, we show the cumulative number density of intervening Si III absorbers as a function of the limiting equivalent width predicted by OWLS (Model AGN). The redshift in the simulation run is higher than the maximum redshift of our data. This is, however, not an issue since we do not expect the gas producing the observed absorption to evolve strongly from $z = 0.25$ to $z = 0.10$. The measured value from this study and from Tilton et al. (2012; T12) and Danforth et al. (2016; D16) are indicated with filled circles. The predicted number density is ~ 1.7 for $\log N(\text{Si III}) > 12.2$ ($\log [W_r(\lambda 1206)/\text{mÅ}] \geq 1.52$), thus only slightly below the observed value of 2.5 ± 0.4 from our COS data set.

It is worth noting that differences between the predicted and observed line-number densities may be alleviated considering that the stellar yields used in the simulations to model the chemical evolution of the gas are uncertain by factors of a few (see Wiersma et al. 2009b). Thus, some modification of the abundances in post-processing would be justified, which would bring the predicted dN/dz into better agreement with our measured value. However, we refrain from doing so because this could break the self-consistency of the simulation if it were to change the cooling rates significantly.

In the lower panel of Fig. 17 we show the phase-space distribution in the temperature-density plane of the Si III-absorbing gas in the AGN run at $z = 0.25$ from OWLS. The typical Si III absorber in the simulation has a temperature of $T \approx 15,000 - 20,000$ K and a density of $n_{\text{H}} \approx 10^{-4} - 10^{-2} \text{ cm}^{-3}$, in very good agreement with the values estimated with Cloudy from the Si II/Si III/Si IV column-density ratios in our COS absorber sample. The resulting range for the expected thermal gas pressure is $P/k \approx 2 - 160 \text{ cm}^{-3} \text{ K}$, thus in a range that is typical for the CGM (Cen 2013).

In conclusion, the AGN model from OWLS and the simulations from Smith et al. (2011) predict absorber properties that are compatible with our observations and in line with the idea, that the majority of the Si III absorbers at $z \leq 0.1$ arise in the extended halos of low-redshift galaxies. For the future, we are planning to further explore the relation between intermediate-ion absorbers and galaxies at low z using higher-resolution simulations from the EAGLE (Evolution and Assembly of GaLaxies and their Environments) project (Schaye et al. 2015).

9. Summary and Conclusions

In this paper, we present a systematic study of intervening Si III absorbers and their relation to galaxies in the redshift

range $z \leq 0.1$ along 303 QSO sightlines using archival UV spectra obtained with *HST*/COS. The main results are summarized as follows:

(1) We detect 69 intervening Si III absorbers in the range $z = 0.00014 - 0.09789$ along a total redshift path of $\Delta z \approx 24$. The restframe equivalent widths in the Si III $\lambda 1206$ line lie in the range $W_r = 13 - 885 \text{ mÅ}$, corresponding to Si III column densities $\log N(\text{Si III}) > 11.9$. We derive a bias-corrected number density of intervening Si III systems of $dN/dz = 2.5 \pm 0.4$ for absorbers with $\log N(\text{Si III}) \geq 12.2$, suggesting that Si III-selected absorbers outnumber strong Mg II at $z \approx 0$ by a factor of ~ 3 . Weak absorbers in the range $\log N(\text{Si III}) = 11.8 - 12.2$ turn out to be rare ($dN/dz \approx 0.3$); they possibly represent an absorber population that is distinct from the one with larger Si III column densities.

(2) The observed Si III absorption is typically accompanied by absorption from other low and/or high ions. The positive correlations between the equivalent widths of Si III and Si IV and between Si III and Si II indicates that doubly ionized silicon traces gas in a range of physical conditions. This conclusion is supported by Cloudy ionization models of the absorbers, which indicate that Si III arises either in diffuse, ionized low-density ($\log n_{\text{H}} \leq -3$, typically) gas that is also observed in Si IV absorption, or in somewhat denser ($\log n_{\text{H}} \geq -3$, typically), more neutral environments that are also traced by Si II.

(3) We geometrically model the absorption cross section of diffuse gas within the virial radii (R_{vir}) of galaxies at $z = 0$ for galaxies in the luminosity range $L/L^* > 0.001$ using the SDSS galaxy luminosity function for $z = 0$ and scaling relations between R_{vir} and L . Our modeling implies that circumgalactic gas within the virial radius of galaxies contributes with $dN/dz < 9$ to the total number density of intervening absorbers, even if a unity covering fraction of the absorbing gas is assumed. If we adopt the SDSS g -band luminosity function as reference (Montero-Dortas et al. 2009), we obtain $dN/dz = 3.6$ as expected number density for CGM absorbers from $L \geq 0.001 L^*$ galaxies. In light of this result, the measured value of $dN/dz(\text{Si III}) = 2.5 \pm 0.4$ is in line with the idea, that the majority of the intervening Si III absorbers with $\log N(\text{Si III}) \geq 12.2$ at $z \approx 0$ trace the circumgalactic medium at $R < R_{\text{vir}}$ of nearby galaxies with an average covering fraction of $\langle f_c \rangle = 2.5/3.6 = 0.69$, a value that is in excellent agreement with results from other studies (Liang & Chen 2014; Werk et al. 2013). Our model further predicts that intervening metal absorbers with number densities $dN/dz > 9$ (e.g., O VI absorbers) must partially arise from gas outside of the virial radius of galaxies.

(4) We compare the Si III absorber redshifts and positions with that of $\sim 64,000$ galaxies at $z \leq 0.1$ using archival galaxy-survey data. For ~ 60 percent of the absorbers we find possible host galaxies with $L \geq 0.01 L^*$ within 300 km s^{-1} of the absorbers and at impact parameters $\rho < 200 \text{ kpc}$, indicating that the spatial distributions of Si III absorbers and galaxies are highly correlated. We verify the significance of this result by studying the distribution of galaxies around the same sightlines in velocity ranges without Si III absorption and find no

clustering of the galaxies, as expected. The observed Si III absorption fraction around the galaxies scales differently with impact parameter than predicted by our model. We assign this behavior to the incompleteness in our galaxy sample to identify faint galaxies that are associated with Si III absorbers.

(5) We estimate the baryon content of the Si III-absorbing gas phase in the CGM at low z using Cloudy ionization models. Assuming that the metallicity of the gas is ≤ 0.5 solar, the cosmological mass density of the gas in Si III absorbers is $\Omega_b(\text{Si III}) \geq 9.2 \times 10^{-4}$. This lower limit is roughly twice the value derived for the H I mass density at $z = 0$, indicating that the diffuse CGM around galaxies, as traced by doubly-ionized Si, contains substantially more baryonic matter than their neutral ISM.

(6) We discuss the origin of intervening Si III absorption in the CGM of galaxies and in galaxy groups and compare our results with previous absorption-line catalogs and CGM studies at low redshift. We suggest that the majority of the strong Si III absorbers with $\log N(\text{Si III}) \geq 12.2$ typically arise within the extended halos of galaxies within R_{vir} , while weak systems with $\log N(\text{Si III}) < 12.2$ possibly also trace gas at larger distances (e.g., group environments or the IGM). The comparison of our measurements with predictions from cosmological hydrodynamical simulations from the OWLS project and other simulations shows a fair agreement for the absorber number density and the estimated temperature-density range of intervening Si III absorbers.

Acknowledgements. This research used the facilities of the Canadian Astronomy Data Centre operated by the National Research Council of Canada with the support of the Canadian Space Agency. This research also has made use of the SIMBAD database, operated at CDS, Strasbourg, France. We thank Joop Schaye and an anonymous referee for helpful comments and suggestions.

References

- Anderson, M.E., & Bregman, J.N. 2011, *ApJ*, 737, 22
- Asplund, M., Grevesse, N., Sauval, A.J., & Scott, P. 2009, *ARA&A*, 47, 481
- Berlind, A.A., Frieman, J., Weinberg, D.H. 2006, *ApJS*, 167, 2006, *ApJS* 167, 1
- Birnboim, Y. & Dekel, A. 2003, *MNRAS*, 345, 349
- Bogdán, Á, Forman, W.R., Kraft, R.P., & Jones, C. 2013, *ApJ*, 772, 98
- Burchett, J.N., Tripp, T.M., Werk, J.K., et al. 2015, *ApJ*, 815, 91
- Calura, F. & Mateucci, F. 2004, *MNRAS*, 350, 351
- Cen, R. 2013, *ApJ*, 770, 139
- Churchill, C.W., Vander Vliet, J.R., Trujillo-Gomez, S., Kacprzak, G.G., & Klypin, A. 2015, *ApJ*, 802, 10
- Collins, J.A., Shull, J.M., & Giroux, M.L. 2009, *ApJ*, 705, 962
- Crain, R.A., McCarthy, I.G., Schaye, J., Theuns, T., & Frenk, C.S. 2013, *MNRAS*, 432, 3005
- Dai, X., Anderson, M.E., Bregman, J.N., & Miller, J.M. 2012, *ApJ*, 755, 107
- Danforth, C.W., Tilton, E.M., Shull, J.M. et al. 2016, *ApJ*, 817, 111
- Debes, J., et al. 2016, *Cosmic Origins Spectrograph Instrument Handbook*, Version 8.0 (Baltimore, MD: STScI)
- Fang, T., & Bryan, G.L. 2001, *ApJ*, 561, 31
- Fangano, A.P.M., Ferrara, A., & Richter, P. 2007, *MNRAS*, 381, 469
- Ferland, G.J., Korista, K.T., Verner, D.A., Fergueson, J.W., Kingdon, J.B., & Verner, E.M. 1998, *PASP*, 110, 761
- Fontana, A., & Ballester, P. 1995, *ESO Messenger*, 80, 37
- Ford, A. B., Davé, R., Oppenheimer, B. D., et al. 2014, *MNRAS*, 444, 1260
- Fox, A.J., Wakker, B.P.; Savage, B.D., et al. 2005, *ApJ*, 630, 332
- Fox, A.J., Savage, B.D., & Wakker, B.P. 2006, *ApJS*, 165, 229
- Fox, A.J., Wakker, B.P., Smoker, J.V., et al. 2010, *ApJ*, 718, 1046
- Green, J.C., Froning, C.S., Osterman, S., et al. 2012, *ApJ*, 744, 60
- Haardt, F., & Madau, P. 2012, *ApJ*, 746, 125
- Herenz, P., Richter, P., Charlton, J.C., & Masiero, J.R. 2013, *A&A*, 550, A87
- Hinshaw, G., Larson, D., Komatsu, E., et al. 2013, *ApJS*, 208, 19
- Kacprzak, G.G., Churchill, C.W., Steidel, C.C., & Murphy, M.T. 2008, *ApJ*, 135, 922
- Kalberla, P.M.W., Burton, W.B., Hartmann, D., et al. 2005, *A&A*, 440, 775
- Keeney, B.A., Stocke, J.T., Rosenberg, J.L., et al. 2013, *ApJ*, 765, 27
- Kereš, D., Katz, N., Weinberg, D.H., & Davé, R. 2005, *MNRAS*, 363, 2
- Kilborn, V.A., Koribalski, B., Forbes, D.A., Barnes, D.G., & Musgrave, R.C. 2005, *MNRAS*, 356, 77
- Lehner, N., Howk, J.C., Thom, C., et al. 2012, *MNRAS*, 424, 2896
- Lehner, N., Howk, J.C., Tripp, T.M., et al. 2013, *ApJ*, 770, 138
- Lehner, N., Howk, J.C., & Wakker, B.P. 2015, *ApJ*, 804, 79
- Liang, C.J., & Chen, H.-W. 2014, *MNRAS*, 445, 2061
- Lundgren, B.F., Brunner, R.J., York, D.G., et al. 2009, *ApJ*, 698, 819
- Mac Low, M.M., & Ferrara, A. 1999, *ApJ*, 513, 142
- Maia, M.A.G., Da Costa, L.N., & Latham, D.W. 1989, *ApJS*, 69, 809
- Maller, A.H., & Bullock, J.S. 2004, *MNRAS*, 355, 694
- Mo, H.J., & Miralda-Escude, J. 1996, *ApJ*, 469, 589
- Montero-Dorta, A.D., & Prada, F. 2009, 399, 1106
- Morton, D.C. 2003, *ApJS*, 149, 205
- Moster, B.P., Somerville, R.S., Maubetsch, C., et al. 2010, *ApJ*, 710, 903
- Nestor, D.B., Turnshek, D.A., & Rao 2005, *ApJ*, 628, 637
- Nielsen, N.M., Churchill, C.W., & Kacprzak, G.G. 2013, *ApJ*, 776, 115
- Nuza, S.E., Parisi, F., & Scannapieco, C. 2014, *MNRAS*, 441, 2593
- Oppenheimer, B., & Davé, R. 2006, *MNRAS*, 373, 1265
- Oppenheimer, B., Davé, R., Katz, N., Kollmeier, J.A., & Weinberg, D.H. 2012, *MNRAS*, 420, 829
- Peacock, J.A., & Smith, R.E. 2000, *MNRAS*, 318, 1144
- Peeples, M.S., Werk, J.K., Tumlinson, J., et al. 2014, *ApJ*, 786, 54
- Planck; Fermi Collaborations, et al. 2015, arXiv: 1502.01589
- Prochaska, J.X., Weiner, B., Chen, H.-W., Mulchaey, J., & Cooksey, K. 2011, *ApJ*, 740, 91
- Prochter, G.E., Prochaska, J.X., Chen, H.-W., et al. 2006, *ApJ*, 639, 766
- Putman, M.E., Peek, J.E.G., & Jounge, M.R. 2012, *ARA&A*, 50, 491

Rauch, M., Sargent, W.L.W., Barlow, T.A., & Carswell, R.F. 2001, *ApJ*, 562, 76

Rees, M.J., Ostriker, J.P., 1977, *MNRAS*, 179, 541

Richter, P., Savage, B.D., Wakker, B.P., Sembach, K.R., Kalberla, P.M.W. 2001, *ApJ*, 549, 281

Richter, P., Fang, T., & Bryan, G. L. 2006, *A&A*, 451, 767

Richter, P. 2006, *Reviews in Modern Astronomy* 19, 31

Richter, P., Charlton, J.C., Fangano, A.P.M., Ben Bekhti, N., & Masiero, J.R. 2009, *ApJ*, 695, 1631

Richter, P., Krause, F., Fechner, C., Charlton, J.C., & Murphy, M.T. 2011, *A&A*, 528, A12

Savage, B.D., & Sembach, K.R. 1991, *ApJ*, 379, 245

Schaye, J., Carswell, R.F., & Kim, T.-S. 2007, *MNRAS*, 379, 1169

Schaye, J., Dalla Vecchia, C., Booth, C.M., et al. 2010, *MNRAS*, 402, 1536

Schaye, J., Crain, R.A., Bower, R.G., et al. 2015, *MNRAS*, 446, 521

Schechter, P. 1976, *ApJ*, 203, 297

Sembach, K.R., Wakker, B.P., Savage, B.D., Richter, P. et al. 2003, *ApJS*, 146, 165

Shull, J.M., Jones, J.R., Danforth, C.W., & Collins, J.A. 2009, 699, 754

Shull, J.M. 2014, *ApJ*, 784, 142

Smith, B.D., Hallman, E.J., Shull, J.M., O’Shea, B.W. 2011, *ApJ*, 731, 6

Stoeke, J.T., Keeney, B.A., Danforth, C.W., et al. 2013, *ApJ*, 763, 148

Stoeke, J.T., Keeney, B.A., Danforth, C.W., et al. 2014, *ApJ*, 791, 128

Tepper-García, T., Richter, P., Schaye, J., et al. 2011, *MNRAS*, 413, 190

Tepper-García, T., Richter, P., Schaye, J., et al. 2012, *MNRAS*, 425, 1640

Tepper-García, T., Richter, P., Schaye, J., et al. 2013, *MNRAS*, 436, 2063

Thom, C., Tumlinson, J., Werk, J., Prochaska, J.X., & Tripp, T. 2012, *ApJ*, 758, 41

Tilton, E.M., Danforth, C.W., Shull, J.M., & Ross, T.L. 2012, *ApJ*, 759, 112

Tripp, T.M., Wakker, B.P., Jenkins, E.B., et al. 2003, *AJ*, 125, 3122

Tripp, T.M., Sembach, K.R., Bowen, D.V., et al. 2008, *ApJS*, 177, 39

Tumlinson, J., Shull, J.M., Rachford, B.L., et al. 2002, *ApJ*, 566, 857

Tumlinson, J., Thom, C., Werk, J.K., et al. 2011, *Sci*, 334, 948

Tumlinson, J., Thom, C., Werk, J.K., et al. 2013, *ApJ*, 777, 59

van de Voort, F., Schaye, J., Booth, C.M., & Dalla Vecchia, C. 2011, *MNRAS*, 414, 2458

Wakker, B.P. & van Woerden, H. 1998, *ARA&A*, 35, 217

Wakker, B.P., Howk, J.C., Savage, B.D. 1999, *Nature*, 402, 388

Wakker, B.P. 2001, *ApJS*, 136, 463

Wakker, B.P., & Savage, B.D. 2009, *ApJS*, 182, 378

Werk, J.K., Prochaska, J.X., Thom, C., et al. 2013, *ApJS*, 204, 17

Werk, J.K., Prochaska, J.X., Tumlinson, J., et al. 2014, *ApJ*, 792, 8

White, S.D.M. & Rees, M.J. 1978, *MNRAS*, 183, 341

Wiersma, R.P.C., Schaye, J., & Smith, B.D. 2009a, *MNRAS*, 393, 99

Wiersma, R.P.C., Schaye, J., Theuns, T., Dalla Vecchia, C., & Tornatore, L. 2009b, *MNRAS*, 399, 574

Zwaan, M.A., van der Hulst, J.M., Briggs, F.H., Verheijen,

M.A.W., & Ryan-Weber, E.V. 2005, *MNRAS*, 364, 1467

Zhu, G. & M’énard, B. 2013, *ApJ*, 770, 130

Appendix A: Supplementary Tables and Figures

[Note: all velocity plots are available in the full version at <http://tucana.astro.physik.uni-potsdam.de/~prichter/si3cgm.pdf>.

Table A.11. Si III candidate systems^a

No.	QSO (COS name)	z_{abs}
1	2MASS-J10131797+0500342	0.046
2	4C-01.61	0.038
3	IRAS01003-2238	0.040
4	MRK1513	0.028
5	PG1112+431	0.018
6	PG1202+281	0.051
7	PHL1811	0.012
8	RXJ0439.6-5311	0.057
9	SDSSJ014143.20+134032.0	0.003
10	SDSSJ024250.85-075914.2	0.005
11	SDSSJ040148.98-054056.5	0.029
12	SDSSJ094331.61+053131.4	0.086
13	SDSSJ101622.60+470643.3	0.057
14	SDSSJ102218.99+013218.8	0.067
15	SDSSJ122018.43+064119.6	0.086
16	SDSSJ150455.56+564920.3	0.036
17	SDSSJ155048.29+400144.9	0.077
18	SDSSJ155304.92+354828.6	0.028
19	SDSSJ161649.42+415416.3	0.089
20	VV2006-J015953.0+134554	0.004

^a detected only in Si III and H I Ly α , but not confirmed in other metal lines.

Table A.1. COS QSO sample - part I

No.	QSO (COS name)	QSO (NED name)	α_{2000}	δ_{2000}	z_{QSO}	Δz_{abs}
1	1ES1028+511	2MASX J10311847+5053358	157.83	50.89	0.360	0.095
2	1ES1553+113	[HB89] 1553+113	238.93	11.19	0.360	0.098
3	1H-2129-624	2MASX J21362313-6224008	324.10	-62.40	0.059	0.041
4	1SAXJ1032.3+5051	2MASSi J1032161+505120	158.07	50.86	0.173	0.098
5	2DFGRSS393Z082	GALEXASC J024500.80-300722.3	41.25	-30.12	0.339	0.098
6	2DFGRSS394Z150 ^a	GALEXASC J024613.27-302942.2	41.56	-30.50	0.131	0.075
7	2E-1058.1+1102	[HB89] 1058+110	165.20	10.77	0.423	0.098
8	2MASS-J09311671+2628474	SDSS J093116.70+262847.4	142.82	26.48	0.781	0.088
9	2MASS-J09512393+3542490	2MASSi J0951239+354248	147.85	35.71	0.399	0
10	2MASS-J09591486+3203573	SDSS J095914.84+320357.2	149.81	32.07	0.565	0.098
11	2MASS-J10131797+0500342	SDSS J101317.98+050034.0	153.32	5.01	0.266	0.096
12	2MASS-J10512569+1247462	SDSS J105125.72+124746.3	162.86	12.80	1.283	0.048
13	2MASS-J11321056+1335091	SDSS J113210.55+133509.2	173.04	13.59	0.201	0.098
14	2MASS-J13250381+2717189	SDSS J132503.79+271718.7	201.27	27.29	0.522	0.085
15	2MASS-J13482237+2456498	SDSS J134822.31+245650.1	207.09	24.95	0.293	0.098
16	2MASS-J14042827+3353426	SDSS J140428.28+335342.6	211.12	33.90	0.550	0.093
17	2MASS-J14294076+0321257	SDSS J142940.73+032125.8	217.42	3.36	0.253	0.098
18	2MASS-J14312586+2442203	FBQS J143125.8+244220	217.86	24.71	0.407	0.098
19	2MASS-J15412146+2817063	SDSS J154121.48+281706.3	235.34	28.29	0.375	0.095
20	2MASX-J01013113+4229356	2MASX J01013113+4229356	15.38	42.49	0.190	0.088
21	2MASX-J15442722+2743237	2MASX J15442722+2743237	236.11	27.72	0.163	0.094
22	3C066A	3C 066A	35.67	43.04	0.444	0.098
23	3C263	3C 263	174.99	65.80	0.646	0.098
24	3C273	3C 273	187.28	2.05	0.158	0.098
25	3C57	3C 057	30.49	-11.54	0.671	0.095
26	4C-01.61	[HB89] 2349-014	357.98	-1.15	0.174	0.098
27	4C-13.41	PG 1004+130	151.86	12.82	0.241	0.098
28	4C63.22	4C +63.22	230.94	63.66	0.204	0.098
29	87GB-142519.5+264555	[HB89] 1425+267	216.90	26.54	0.364	0.085
30	AKN-564	UGC 12163	340.66	29.73	0.025	0.006
31	B0117-2837	2MASSi J0119356-282131	19.90	-28.36	0.349	0.095
32	BZBJ1001+2911	2MASS J10011021+2911376	150.29	29.19	0.558	0.095
33	CAL-F-COPY	2MASX J05030396-6633456	75.77	-66.56	0.064	0.046
34	CSO712	SBS 1459+554	225.13	55.29	0.405	0.097
35	ESO-031-G-008	ESO 031- G 008	46.90	-72.83	0.028	0.008
36	ESO-141-55	ESO 141- G 055	290.31	-58.67	0.037	0.019
37	ESO267-013	ESO 267- G 013	181.22	-43.73	0.015	0
38	FBQS-0751+2919	FBQS J0751+2919	117.80	29.33	0.916	0.098
39	FBQSJ1010+3003	FBQS J1010+3003	152.50	30.06	0.256	0.098
40	FBS1526+659	SDSS J152728.65+654810.4	231.87	65.80	0.345	0.098
41	FIRST-J020930.7-043826	FBQS J0209-0438	32.38	-4.64	1.128	0.052
42	H1821+643	[HB89] 1821+643	275.49	64.34	0.297	0.098
43	HB89-0107-025-NED05	[HB89] 0107-025 NED05	17.57	-2.31	0.956	0.098
44	HB89-0202-765	[HB89] 0202-765	30.56	-76.33	0.389	0.098
45	HB89-0232-042	[HB89] 0232-042	38.78	-4.03	1.437	0.090
46	HE0056-3622	[HB89] 0056-363	14.66	-36.10	0.164	0.088
47	HE0153-4520	6dF J0155132-450612	28.81	-45.10	0.451	0.098
48	HE0226-4110	IRAS 02262-4110	37.06	-40.95	0.493	0.095
49	HE0238-1904	2MASSi J0240325-185151	40.14	-18.86	0.631	0.098
50	HE0435-5304	HE 0435-5304	69.21	-52.98	1.231	0.098
51	HE0439-5254	HE 0439-5254	70.05	-52.81	1.053	0.095
52	HE1159-1338	CTS 0308	180.49	-13.92	0.506	0.098
53	HE2347-4342	CTS 0498	357.64	-43.43	2.885	0.095
54	HS-0033+4300	HS 0033+4300	9.10	43.28	0.120	0.088
55	HS1102+3441	TON 1329	166.42	34.43	0.508	0.098
56	HS1831+5338	HS 1831+5338	278.21	53.67	0.039	0.020
57	IO-AND	IO And	12.08	39.69	0.134	0.093
58	IRAS-F04250-5718	IRAS F04250-5718	66.50	-57.20	0.104	0.086
59	IRAS-F22456-5125	2MASX J22484165-5109338	342.17	-51.16	0.100	0.082
60	IRAS-L06229-6434	2MASX J06230765-6436211	95.78	-64.61	0.129	0.088
61	IRAS01003-2238	IRAS 01003-2238	15.71	-22.37	0.118	0.093
62	IRAS08339+6517	2MASX J08382309+6507160	129.60	65.12	0.019	0.001
63	IRAS10257-4339	NGC 3256	156.96	-43.90	0.009	0
64	IRAS11598-0112	2MASX J12022678-0129155	180.61	-1.49	0.151	0.093
65	IRAS16104+5235	NGC 6090	242.92	52.46	0.029	0
66	IRAS23133-4251	NGC 7552	349.05	-42.58	0.005	0
67	IZW18-OBJECT-1	UGCA 166	143.51	55.24	0.003	0
68	J102548.47+362258.4	SDSS J102548.38+362258.4	156.45	36.38	0.126	0.088
69	J111244.15+550347.1	SDSS J111244.05+550347.0	168.18	55.06	0.132	0.076
70	J141612.96+122340.5	SDSS J141612.87+122340.4	214.05	12.39	0.123	0.074
71	J142947.03+064334.9	SDSS J142947.00+064334.9	217.45	6.73	0.174	0.085
72	KISSR1578	MRK 0259	202.18	43.93	0.028	0.010
73	KISSR242	TON 0151	199.02	29.38	0.038	0.017
74	LBQS-0107-0235	LBQS 0107-0235	17.55	-2.33	0.957	0.098
75	LBQS-1435-0134	LBQS 1435-0134	219.45	-1.79	1.311	0.096
76	MARK509	MRK 0509	311.04	-10.72	0.034	0.011

^a Spectrum shows no QSO characteristics; possibly wrong source (white dwarf) observed; not considered in study.

Table A.2. COS QSO sample - part II

No.	QSO (COS name)	QSO (NED name)	α_{2000}	δ_{2000}	z_{QSO}	Δz_{abs}
77	MCG+10-22-028	VV 487	234.54	57.60	0.073	0.055
78	MR2251-178	MR 2251-178	343.52	-17.58	0.064	0.046
79	MRK-1044	MRK 1044	37.52	-9.00	0.016	0
80	MRK-279	UGC 08823	208.26	69.31	0.030	0.012
81	MRK106	MRK 0106	139.98	55.36	0.123	0.092
82	MRK1513	UGC 11763	323.12	10.14	0.063	0.045
83	MRK290	MRK 0290	233.97	57.90	0.030	0.010
84	MRK335	MRK 0335	1.58	20.20	0.026	0.007
85	MRK380	MRK 0380	109.96	74.47	0.475	0.095
86	MRK421	MRK 0421	166.11	38.21	0.030	0.012
87	MRK486	MRK 0486	234.16	54.56	0.039	0.020
88	MRK504	MRK 0504	255.28	29.41	0.036	0.016
89	MRK595	MRK 0595	40.40	7.19	0.027	0.007
90	MRK817	UGC 09412	219.09	58.79	0.031	0.014
91	MRK876	MRK 0876	243.49	65.72	0.129	0.095
92	NGC-3516	NGC 3516	166.70	72.57	0.009	0
93	NGC-3783	NGC 3783	174.76	-37.74	0.010	0
94	NGC-4051	NGC 4051	180.79	44.53	0.002	0
95	NGC-5548	NGC 5548	214.50	25.14	0.017	0
96	NGC-7469	NGC 7469	345.82	8.87	0.016	0
97	NGC3125-1	NGC 3125	151.64	-29.93	0.004	0
98	NGC3690-OBJECT-1	NGC 3690	172.13	58.56	0.010	0
99	NGC4670-OBJECT-1	NGC 4670	191.32	27.13	0.004	0
100	NPM1G+68.0125	2MASX J15085291+6814074	227.22	68.24	0.059	0.041
101	PG-1148+549	SBS 1148+549	177.84	54.63	0.976	0.098
102	PG-1206+459	PG 1206+459	182.24	45.68	1.165	0.030
103	PG-1338+416	PG 1338+416	205.25	41.39	1.217	0.059
104	PG-1407+265	FBQS J140923.9+261821	212.35	26.31	0.940	0.098
105	PG-1522+101	[HB89] 1522+101	231.10	9.97	1.328	0.095
106	PG-1630+377	[HB89] 1630+377	248.01	37.63	1.479	0.098
107	PG0003+158	PG 0003+158	1.50	16.16	0.451	0.098
108	PG0804+761	PG 0804+761	122.74	76.05	0.100	0.082
109	PG0832+251	FBQS J083535.8+245940	128.90	24.99	0.330	0.098
110	PG0953+414	PG 0953+414	149.22	41.26	0.234	0.093
111	PG1001+291	PG 1001+291	151.01	28.93	0.327	0
112	PG1011-040	PG 1011-040	153.59	-4.31	0.058	0.040
113	PG1048+342	PG 1048+342	162.93	33.99	0.167	0.095
114	PG1049-005	PG 1049-005	162.96	-0.85	0.360	0.098
115	PG1112+431	PG 1112+431	168.77	42.83	0.301	0.098
116	PG1115+407	PG 1115+407	169.63	40.43	0.154	0.098
117	PG1116+215	PG 1116+215	169.79	21.32	0.176	0.092
118	PG1121+422	PG 1121+422	171.16	42.03	0.225	0.098
119	PG1202+281	GQ Com	181.18	27.90	0.165	0.098
120	PG1259+593	SBS 1259+593	195.30	59.04	0.478	0.093
121	PG1424+240	FBQS J142700.4+234800	216.75	23.80	0.160	0.098
122	PG1626+554	SBS 1626+554	246.98	55.38	0.133	0.095
123	PHL1811	FBQS J2155-0922	328.76	-9.37	0.190	0.098
124	PKS0405-123	[HB89] 0405-123	61.95	-12.19	0.573	0
125	PKS0552-640	PKS 0552-640	88.11	-64.03	0.680	0.082
126	PKS0558-504	[HB89] 0558-504	89.95	-50.45	0.137	0.094
127	PKS0637-752	[HB89] 0637-752	98.94	-75.27	0.653	0.086
128	PKS1101-325	[HB89] 1101-325	165.88	-32.85	0.356	0.098
129	PKS1136-13	[HB89] 1136-135	174.79	-13.85	0.556	0.089
130	PKS1302-102	PG 1302-102	196.39	-10.56	0.278	0.095
131	PKS2005-489	[HB89] 2005-489	302.36	-48.83	0.071	0.052
132	PKS2155-304	[HB89] 2155-304	329.72	-30.23	0.116	0.098
133	PMNJ1103-2329	2MASX J11033765-2329307	165.91	-23.49	0.186	0.098
134	Q0302-003	LBQS 0302-0019	46.21	-0.14	3.297	0.030
135	Q0439-433	[HB89] 0439-433	70.32	-43.23	0.594	0.093
136	Q2128-123	[HB89] 2128-123	322.90	-12.12	0.501	0.017
137	Q2251+155	3C 454.3	343.49	16.15	0.859	0.082
138	QSO-B0026+129	PG 0026+129	7.31	13.27	0.142	0.098
139	QSO-B0157+001	MRK 1014	29.96	0.39	0.163	0.098
140	QSO-B0844+349	PG 0844+349	131.93	34.75	0.064	0.046
141	QSO-B0906+3248	TON 1009	137.28	32.61	0.810	0.098
142	QSO-B0923+201	FBQS J092554.7+400414	141.48	40.07	0.472	0.094
143	QSO-B1124+271	FBQS J1127+2654	171.90	26.91	0.379	0.098
144	QSO-B1126-041	MRK 1298	172.32	-4.40	0.062	0.044
145	QSO-B1139+305	[HB89] 1139+305	175.55	30.27	0.482	0.098
146	QSO-B1229+204	MRK 0771	188.01	20.16	0.063	0.045
147	QSO-B1254+571	SDSS J125614.10+565225.3	194.06	56.87	0.041	0.023
148	QSO-B1307+085	PG 1307+085	197.45	8.33	0.155	0.098
149	QSO-B1309+3531	FBQS J131217.7+351521	198.07	35.26	0.183	0.098
150	QSO-B1435-0645	[HB89] 1435-067	219.57	-6.97	0.126	0.098
151	QSO-B1617+1731	MRK 0877	245.05	17.41	0.112	0.094
152	QSO-B2214+139	MRK 0304	334.30	14.24	0.066	0.047

Table A.3. COS QSO sample - part III

No.	QSO (COS name)	QSO (NED name)	α_{2000}	δ_{2000}	z_{QSO}	Δz_{abs}
153	RBS144	SARS 014.56153-51.50151	15.11	-51.23	0.063	0.033
154	RBS1892	IRAS F22423-4707	341.33	-46.87	0.200	0.088
155	RBS563	6dF J0438292-614759	69.62	-61.80	0.069	0.045
156	RXJ0439.6-5311	6dF J0439387-531131	69.91	-53.19	0.243	0.098
157	RXJ07145+7408	2MASSi J0714362+740810	108.65	74.14	0.371	0.095
158	RXJ1230.8+0115	SDSS J123050.03+011522.6	187.71	1.26	0.117	0.098
159	RXJ2154.1-4414	6dF J2154511-441406	328.71	-44.23	0.344	0.098
160	RXS-J00057-5007	2MASX J00054309-5006550	1.43	-50.12	0.033	0.014
161	RXSJ09565-0452	2MASX J09563012-0453174	149.13	-4.89	0.150	0.095
162	RXSJ15032+6809	2MASX J15031625+6810067	225.82	68.17	0.114	0.096
163	RXSJ16083+6018	2MASX J16082057+6018281	242.09	60.31	0.178	0.098
164	SBS0335-052-OBJECT-1	SBS 0335-052	54.43	-5.04	0.014	0
165	SBS1108+560	SBS 1108+560	167.88	55.79	0.767	0.073
166	SBS1122+594	SBS 1122+594	171.47	59.17	0.851	0.098
167	SBS1415+437-OBJECT-1	SBS 1415+437	214.26	43.50	0.002	0
168	SBS1458+534	SBS 1458+535	224.96	53.32	0.338	0.098
169	SBS1521+598	SBS 1520+598	230.47	59.67	0.286	0.098
170	SBS1624+575	SBS 1624+575	246.36	57.46	0.067	0.049
171	SDSS-J082354.96+280621.6	KUG 0820+282	125.98	28.11	0.047	0.009
172	SDSS-J090704.88+532656.6	SHOC 240	136.77	53.45	0.030	0.007
173	SDSS-J093001.90+284858.4	SDSS J093001.90+284858.4	142.51	28.82	0.487	0.088
174	SDSS-J093706.85+170021.5	SDSS J093706.85+170021.5	144.28	17.01	0.506	0.095
175	SDSS-J100535.24+013445.7	SDSS J100535.24+013445.7	151.40	1.58	1.081	0.095
176	SDSS-J103304.86+211216.1	SDSS J103304.86+211216.1	158.27	21.20	0.315	0.098
177	SDSS-J115552.80+292238.4	SDSS J115552.80+292238.4	178.97	29.38	0.520	0.092
178	SDSS-J124129.64+285212.0	SDSS J124129.64+285212.0	190.37	28.87	0.590	0.098
179	SDSS-J131802.01+262830.3	SDSS J131802.01+262830.3	199.51	26.48	1.236	0.098
180	SDSS-J135424.90+243006.3	SDSS J135424.90+243006.3	208.60	24.50	1.893	0.092
181	SDSS-J135726.27+043541.4	[HB89] 1354+048	209.36	4.59	1.235	0.092
182	SDSS-J145424.33+304658.3	SDSS J145424.33+304658.3	223.60	30.78	0.466	0.093
183	SDSS-J150928.29+070235.7	SDSS J150928.29+070235.7	227.37	7.04	0.419	0.095
184	SDSS-J150952.19+111047.0	SDSS J150952.19+111047.0	227.47	11.18	0.285	0.093
185	SDSS-J151237.05+012846.6	SDSS J151237.05+012846.6	228.15	1.48	0.266	0.098
186	SDSS-J151507.43+065708.3	SDSS J151507.43+065708.3	228.78	6.95	0.268	0.098
187	SDSS-J160519.70+144852.2	SDSS J160519.70+144852.2	241.33	14.81	0.372	0.085
188	SDSSJ001224.01-102226.5	FBQS J0012-1022	3.10	-10.37	0.228	0.098
189	SDSSJ004222.29-103743.8	SDSS J004222.29-103743.6	10.59	-10.63	0.425	0.088
190	SDSSJ005527.46-002148.7	LBQS 0052-0038	13.86	-0.36	0.168	0.093
191	SDSSJ014143.20+134032.0	2MASX J01414319+1340328	25.43	13.68	0.045	0.026
192	SDSSJ015530.02-085704.0	SDSS J015530.01-085704.0	28.88	-8.95	0.164	0.098
193	SDSSJ022614.46+001529.7	SDSS J022614.46+001529.7	36.56	0.26	0.616	0.098
194	SDSSJ024250.85-075914.2	2MASSi J0242508-075914	40.71	-7.99	0.378	0.098
195	SDSSJ025937.46+003736.3	LBQS 0257+0025	44.91	0.63	0.535	0.098
196	SDSSJ040148.98-054056.5	SDSS J040148.97-054056.6	60.45	-5.68	0.571	0.095
197	SDSSJ080908.13+461925.6	SDSS J080908.13+461925.5	122.28	46.32	0.659	0.098
198	SDSSJ082024.21+233450.4	SDSS J082024.21+233450.4	125.10	23.58	0.471	0.098
199	SDSSJ082633.51+074248.3	SDSS J082633.51+074248.3	126.64	7.71	0.311	0.098
200	SDSSJ084349.49+411741.6	SDSS J084349.49+411741.6	130.96	41.29	0.991	0.098
201	SDSSJ091235.42+295725.4	SDSS J091235.42+295725.4	138.15	29.96	0.306	0.098
202	SDSSJ091440.38+282330.6	SDSS J091440.38+282330.6	138.67	28.39	0.735	0.098
203	SDSSJ092554.43+453544.4	SDSS J092554.43+453544.4	141.48	45.60	0.330	0.095
204	SDSSJ092600.4+442736.1	SDSS J092600.40+442736.1	141.50	44.46	0.181	0.093
205	SDSSJ092837.98+602521.0	SBS 0924+606B	142.16	60.42	0.296	0.098
206	SDSSJ092909.79+464424.0	2MASX J09290975+4644235	142.29	46.74	0.240	0.098
207	SDSSJ093518.19+020415.5	[HB89] 0932+022	143.83	2.07	0.649	0.098
208	SDSSJ093813.49+542825.0	SBS 0934+546	144.56	54.47	0.102	0.052
209	SDSSJ094331.61+053131.4	SDSS J094331.61+053131.4	145.88	5.53	0.564	0.098
210	SDSSJ094733.21+100508.7	2MASX J09473320+1005093	146.89	10.09	0.140	0.098
211	SDSSJ094952.91+390203.9	2MASSi J0949529+390203	147.47	39.03	0.366	0.098
212	SDSSJ095000.73+483129.3	SDSS J095000.73+483129.3	147.50	48.52	0.589	0.098
213	SDSSJ095109.12+330745.8	SDSS J095109.12+330745.8	147.79	33.13	0.645	0.091
214	SDSSJ095915.65+050355.1	SDSS J095915.65+050355.1	149.82	5.07	0.163	0.098
215	SDSSJ100102.55+594414.3	SBS 0957+599	150.26	59.74	0.747	0.095
216	SDSSJ100902.06+071343.8	SDSS J1009+0713	152.26	7.23	0.457	0.048
217	SDSSJ101622.60+470643.3	SDSS J101622.60+470643.3	154.09	47.11	0.822	0.088
218	SDSSJ102218.99+013218.8	LBQS 1019+0147	155.58	1.54	0.790	0.098
219	SDSSJ104709.83+130454.6	SDSS J104709.83+130454.6	161.79	13.08	0.401	0.095
220	SDSSJ104816.25+120734.7	SDSS J104816.25+120734.7	162.07	12.13	0.291	0.095
221	SDSSJ104843.49+130605.9	SDSS J104843.49+130605.9	162.18	13.10	0.219	0.094
222	SDSSJ105945.23+144142.9	SDSS J105945.23+144142.9	164.94	14.70	0.632	0.098
223	SDSSJ105958.82+251708.8	SDSS J105958.82+251708.8	164.99	25.29	0.663	0.098
224	SDSSJ110312.93+414154.9	2MASS J11031293+4141549	165.80	41.70	0.403	0.098
225	SDSSJ110406.94+314111.4	TON 0052	166.03	31.69	0.436	0.098
226	SDSSJ111239.11+353928.2	SDSS J111239.11+353928.2	168.16	35.66	0.636	0.098
227	SDSSJ111754.31+263416.6	TON 0576	169.48	26.57	0.422	0.098
228	SDSSJ112114.22+032546.7	SDSS J112114.21+032546.8	170.31	3.43	0.152	0.092

Table A.4. COS QSO sample - part IV

No.	QSO (COS name)	QSO (NED name)	α_{2000}	δ_{2000}	z_{QSO}	Δz_{abs}
229	SDSSJ112244.89+575543.0	SDSS J112244.87+575543.1	170.69	57.93	0.907	0.098
230	SDSSJ113327.78+032719.1	SDSS J113327.78+032719.1	173.37	3.46	0.525	0.098
231	SDSSJ113457.62+255527.9	FBQS J113457.6+255527	173.74	25.92	0.710	0.098
232	SDSSJ115758.72-002220.8	SDSS J115758.72-002220.7	179.49	-0.37	0.260	0.098
233	SDSSJ120556.08+104253.8	[HB89] 1203+109	181.48	10.72	1.089	0.093
234	SDSSJ120720.99+262429.1	SDSS J120720.99+262429.1	181.84	26.41	0.322	0.098
235	SDSSJ121037.56+315706.0	SDSS J121037.56+315706.0	182.66	31.95	0.389	0.098
236	SDSSJ121114.56+365739.5	SDSS J121114.56+365739.5	182.81	36.96	0.171	0.098
237	SDSSJ121430.55+082508.1	LBQS 1211+0841	183.63	8.42	0.586	0.092
238	SDSSJ121640.56+071224.3	SDSS J121640.56+071224.3	184.17	7.21	0.588	0.090
239	SDSSJ121716.08+080942.0	LBQS 1214+0826	184.32	8.16	0.344	0.095
240	SDSSJ121850.51+101554.2	LBQS 1216+1032	184.71	10.27	0.543	0.096
241	SDSSJ122018.43+064119.6	2MASS J12201843+0641196	185.08	6.69	0.287	0.090
242	SDSSJ122035.10+385316.4	FBQS J1220+3853	185.15	38.89	0.377	0.095
243	SDSSJ122102.49+155447.0	LBQS 1218+1611	185.26	15.91	0.229	0.090
244	SDSSJ122312.16+095017.7	LBQS 1220+1006	185.80	9.84	0.277	0.088
245	SDSSJ122317.79+092306.9	LBQS 1220+0939	185.82	9.39	0.682	0.098
246	SDSSJ122512.93+121835.6	LBQS 1222+1235	186.30	12.31	0.412	0.093
247	SDSSJ122520.13+084450.7	LBQS 1222+0901	186.33	8.75	0.535	0.088
248	SDSSJ123304.05-003134.1	LBQS 1230-0015	188.27	-0.53	0.471	0.098
249	SDSSJ123335.07+475800.4	2MASS J1233350+475800	188.40	47.97	0.382	0.098
250	SDSSJ123426.80+072411.3	SDSS J123426.80+072411.3	188.61	7.40	0.845	0.090
251	SDSSJ124154.02+572107.3	SDSS J124154.02+572107.3	190.48	57.35	0.583	0.098
252	SDSSJ124511.25+335610.1	FBQS J124511.2+335610	191.30	33.94	0.712	0.075
253	SDSSJ132222.68+464535.2	SDSS J132222.68+464535.2	200.59	46.76	0.375	0.098
254	SDSSJ133045.15+281321.4	SDSS J133045.15+281321.4	202.69	28.22	0.417	0.098
255	SDSSJ133053.27+311930.5	[HB89] 1328+315	202.72	31.33	0.242	0.098
256	SDSSJ134206.56+050523.8	[HB89] 1339+053	205.53	5.09	0.264	0.098
257	SDSSJ134231.22+382903.4	SDSS J134231.22+382903.4	205.63	38.48	0.172	0.098
258	SDSSJ134246.89+184443.6	SDSS J134246.89+184443.6	205.70	18.75	0.383	0.098
259	SDSSJ134251.60-005345.3	LBQS 1340-0038	205.71	-0.90	0.327	0.098
260	SDSSJ135625.55+251523.7	SDSS J135625.55+251523.7	209.11	25.26	0.164	0.098
261	SDSSJ135712.61+170444.1	2MASX J13571258+1704438	209.30	17.08	0.150	0.098
262	SDSSJ140732.25+550725.6	SDSS J140732.25+550725.4	211.88	55.12	1.028	0.098
263	SDSSJ141542.90+163413.8	SDSS J141542.90+163413.7	213.93	16.57	0.743	0.092
264	SDSSJ141910.20+420746.9	SDSS J141910.20+420746.8	214.79	42.13	0.875	0.098
265	SDSSJ143511.53+360437.2	SDSS J143511.53+360437.2	218.80	36.08	0.430	0.090
266	SDSSJ143726.14+504555.8	SBS 1435+509	219.36	50.77	0.782	0.098
267	SDSSJ144511.28+342825.4	SDSS J144511.28+342825.4	221.30	34.47	0.697	0.088
268	SDSSJ145108.76+270926.9	PG 1448+273	222.79	27.16	0.065	0.047
269	SDSSJ145907.58+714019.9	3C 309.1	224.78	71.67	0.905	0.095
270	SDSSJ150455.56+564920.3	SBS 1503+570	226.23	56.82	0.359	0.097
271	SDSSJ151428.64+361957.9	SDSS J151428.64+361957.9	228.62	36.33	0.695	0.031
272	SDSSJ152139.66+033729.2	SDSS J152139.66+033729.2	230.41	3.62	0.126	0.098
273	SDSSJ155048.29+400144.9	SDSS J155048.29+400144.8	237.70	40.03	0.497	0.098
274	SDSSJ155304.92+354828.6	SDSS J155304.92+354828.6	238.27	35.81	0.723	0.098
275	SDSSJ155504.39+362848.0	SDSS J155504.39+362847.9	238.77	36.48	0.714	0.098
276	SDSSJ161649.42+415416.3	SDSS J161649.42+415416.3	244.21	41.90	0.441	0
277	SDSSJ161916.54+334238.4	SDSS J161916.54+334238.4	244.82	33.71	0.472	0.098
278	SDSSJ171737.95+655939.3	SDSS J171737.94+655939.3	259.41	65.99	0.293	0.098
279	SDSSJ172823.40+573243.0	NGC 6387	262.10	57.55	0.028	0
280	SDSSJ225738.20+134045.4	SDSS J225738.20+134045.4	344.41	13.68	0.595	0.098
281	TON236	[HB89] 1526+285	232.17	28.42	0.450	0.098
282	TON580	TON 0580	172.79	31.23	0.289	0.098
283	TONS210	TON S210	20.46	-28.35	0.116	0.098
284	UGCA-166	UGCA 166	143.51	55.24	0.003	0
285	UKS-0242-724	UKS 0242-724	40.79	-72.28	0.102	0.076
286	UM428	UM 428	171.67	-1.69	0.046	0.023
287	VIIZW244	VII Zw 244	131.19	76.89	0.131	0.098
288	VV2000-J093603.9+320709	FBQS J093603.8+320709	144.02	32.12	1.152	0.064
289	VV2000-J150204.1+064514	SDSS J150204.10+064516.0	225.52	6.75	0.286	0.098
290	VV2006-J015953.0+134554	SDSS J015952.95+134554.3	29.97	13.77	0.504	0.098
291	VV2006-J080838.8+051440	SDSS J080838.84+051439.9	122.16	5.24	0.361	0.098
292	VV2006-J085259.2+031320	2MASX J08525919+0313200	133.25	3.22	0.297	0.098
293	VV2006-J091431.8+083742	SDSS J091431.77+083742.7	138.63	8.63	0.649	0.098
294	VV2006-J105910.9+051935	SDSS J105910.89+051935.3	164.79	5.33	0.756	0.098
295	VV2006-J105956.1+121151	SDSS J105956.14+121151.1	164.98	12.20	0.993	0.094
296	VV2006-J111507.6+023757	SDSS J111507.65+023757.5	168.78	2.63	0.567	0.098
297	VV2006-J112005.0+041323	SDSS J112004.99+041323.2	170.02	4.22	0.547	0.098
298	VV2006-J112224.1+031802	SDSS J112224.15+031802.5	170.60	3.30	0.475	0.098
299	VV2006-J125124.6+055420	SDSS J125124.65+055420.2	192.85	5.91	1.385	0.081
300	VV2006-J130524.3+035731	SDSS J130524.25+035730.9	196.35	3.96	0.546	0.098
301	VV2006-J131545.2+152556	SDSS J131545.20+152556.3	198.94	15.43	0.448	0.098
302	VV2006-J140655.7+015713	SDSS J140655.66+015712.8	211.73	1.95	0.427	0.098
303	VV96-J100254.6+324039	FBQS J100254.5+324038	150.73	32.68	0.828	0.098

Table A.5. Absorption-line systems - part I

No.	QSO (COS name)	z_{abs}	Ion	W_r^a [mÅ]	ΔW_r [mÅ]	$\log N$	$\Delta(\log N)$
1	2DFGRSS393Z082	0.004	H I	563	29		
2			Si II	33	12	12.49	0.25
3			Si III	69	27	12.91	0.15
4			Si IV	120		12.68	
5			C II	53	18	13.53	0.23
6			C IV				
7	2MASS-J10512569+1247462	0.003	H I	1027	103		
8			Si II				
9			Si III	190	32	13.13	0.12
10			Si IV	88	26	13.17	0.15
11			C II	101	22	13.83	0.15
12			C IV				
13	3C066A	0.067	H I	879	15		
14			Si II	19		11.94	
15			Si III	76	8	12.59	0.07
16			Si IV				
17			C II	21	8	13.03	0.22
18			C IV				
19	3C263	0.064	H I	1048	10		
20			Si II	24	4	12.23	0.11
21			Si III	163	12	12.93	0.04
22			Si IV	329	13	13.68	
23			C II	60	9	13.46	0.06
24			C IV	352	18	14.06	
25	3C273	0.005	H I	356	13		
26			Si II	10	4	11.87	0.11
27			Si III	20	3	12.03	0.04
28			Si IV	13		11.54	
29			C II	10	3	12.70	0.13
30			C IV				
31	3C57	0.053	H I	789	11		
32			Si II	3		11.66	
33			Si III	50	10	12.41	0.09
34			Si IV	50	11	12.77	0.14
35			C II				
36			C IV	173	27	13.73	0.09
37	HE0056-3622	0.043	H I	749	12		
38			Si II	15		11.63	
39			Si III	36	6	12.24	0.11
40			Si IV	11		12.12	
41			C II				
42			C IV	138	21	13.57	0.08
43	HE0439-5254	0.006	H I	481	14		
44			Si II	148		12.60	
45			Si III	153	8	13.10	
46			Si IV	48	9	12.79	0.13
47			C II	82	11	13.72	0.09
48			C IV	130	13	13.20	0.12
49	IRAS-F04250-5718	0.004	H I	830	9		
50			Si II	28	3	12.33	0.06
51			Si III	110	7	12.78	0.03
52			Si IV	12	4	12.21	0.11
53			C II	103	3	13.75	0.01
54			C IV	55	8	13.17	0.07
55	IRAS11598-0112	0.021	H I	1052	60		
56			Si II	204	69	13.44	0.11
57			Si III	377	52	13.43	
58			Si IV	231	55	13.62	0.09
59			C II				
60			C IV				
61	PG-1148+549	0.003	H I	375	8		
62			Si II	15		11.63	
63			Si III	38	4	12.32	0.08
64			Si IV	11		12.12	
65			C II				
66			C IV	84	10	13.43	0.08
67	PG-1630+377	0.024	H I	579	9		
68			Si II	15		11.63	
69			Si III	40	8	12.34	0.07
70			Si IV				
71			C II	47	9	13.38	0.09
72			C IV	40	21	13.18	0.16

^a Used transitions: H I $\lambda 1215$, Si II $\lambda 1260$, Si III $\lambda 1206$, Si IV $\lambda 1393$, C II $\lambda 1334$, and C IV $\lambda 1548$.

Table A.6. Absorption-line systems - part II

No.	QSO (COS name)	z_{abs}	Ion	W_r [mÅ]	ΔW_r [mÅ]	$\log N$	$\Delta(\log N)$
73	PG0832+251	0.028	H I	325	18		
74			Si II	48	12	12.59	0.20
75			Si III	40	8	12.35	0.16
76			Si IV	j13		j12.25	
77			C II	39	6	13.33	0.11
78	PG0832+251	0.017	C IV	34	12	13.03	0.20
79			H I	1718	26		
80			Si II	462	22	j13.88	
81			Si III	885	37	j13.93	
82			Si IV	526	27	j13.97	
83	PG1048+342	0.059	C II	734	38	j14.89	
84			C IV	1114	60	j14.73	
85			H I	321	23		
86			Si II	j5		j11.63	
87			Si III	88	20	12.68	0.09
88	PG1049-005	0.038	Si IV	j11		j12.12	
89			C II	18	3	12.95	0.08
90			C IV	48	17	13.16	0.13
91			H I	592	28		
92			Si II	j40		j12.68	
93	PG1259+593	0.046	Si III	169	25	12.98	0.08
94			Si IV	j20		j12.52	
95			C II				
96			C IV	68	32	13.35	0.20
97			H I	1040	15		
98	PHL1811	0.081	Si II	25	5	12.33	0.09
99			Si III	103	5	12.75	0.04
100			Si IV	25	5	12.45	0.12
101			C II				
102			C IV	121	12	13.53	0.07
103	PHL1811	0.078	H I	940	13		
104			Si II	178	4	j13.29	
105			Si III	219	5	j13.28	
106			Si IV	133	9	13.24	0.04
107			C II	140	6	13.93	0.03
108	PHL1811	0.074	C IV	220	16	13.81	0.05
109			H I	456	15		
110			Si II	27	6	12.28	0.10
111			Si III	43	5	12.30	0.09
112			Si IV	j12		j12.34	
113	PHL1811	0.074	C II	34	4	13.19	0.07
114			C IV	18	12	12.76	0.18
115			H I	508	9		
116			Si II	j35		j12.34	
117			Si III	57	9	12.43	0.08
118	PKS1101-325	0.070	Si IV	12	10	12.39	0.12
119			C II	9	5	12.73	0.18
120			C IV	41	21	13.17	0.11
121			H I	535	20		
122			Si II	32	10	12.36	0.17
123	PKS1302-102	0.095	Si III	68	10	12.54	0.10
124			Si IV				
125			C II				
126			C IV				
127			H I	481	14		
128	PKS1302-102	0.042	Si II	36	8	12.41	0.11
129			Si III	156	10	12.89	0.04
130			Si IV	j21		j12.40	
131			C II	53	9	13.40	0.09
132			C IV	50	18	13.20	0.12
133	PKS1302-102	0.004	H I	488	12		
134			Si II	j6		j11.87	
135			Si III	50	5	12.42	0.07
136			Si IV	11	3	12.29	0.24
137			C II	16	6	12.94	0.20
138	PKS1302-102	0.004	C IV	45	13	13.10	0.19
139			H I	321	13		
140			Si II	j10		j11.87	
141			Si III	34	5	12.26	0.11
142			Si IV	j10		j12.44	
143	PKS1302-102	0.004	C II	9	4	12.82	0.18
144			C IV	20	5	12.78	0.12

Table A.7. Absorption-line systems - part III

No.	QSO (COS name)	z_{abs}	Ion	W_r [mÅ]	ΔW_r [mÅ]	$\log N$	$\Delta(\log N)$
145	PKS2005-489	0.017	H I	311	8		
146			Si II	112		11.98	
147			Si III	14	7	11.95	0.22
148			Si IV	111		12.42	
149			C II	10	5	12.80	0.22
150	PMNJ1103-2329	0.084	C IV	70	20	13.34	0.17
151			H I	965	29		
152			Si II	50	12	12.59	0.13
153			Si III	219	21	13.15	
154			Si IV	152	26	13.31	0.10
155	PMNJ1103-2329	0.004	C II	84	12	13.66	0.10
156			C IV	411	39	14.19	
157			H I	587	20		
158			Si II	112		11.92	
159			Si III	101	16	12.86	0.13
160	QSO-B1139+305	0.032	Si IV	46	9	12.80	0.12
161			C II	13	8	13.04	0.23
162			C IV	271	28	14.04	
163			H I	905	34		
164			Si II	140		12.68	
165	RXJ1230.8+0115	0.078	Si III	248	27	13.23	0.10
166			Si IV	130		12.72	
167			C II	96	30	13.95	0.12
168			C IV				
169			H I	438	4		
170	RXJ1230.8+0115	0.006	Si II		6	12.41	0.06
171			Si III	56	4	12.42	0.09
172			Si IV	25			
173			C II		7	14.05	
174			C IV	304			
175	RXJ2154.1-4414	0.062	H I	605	6		
176			Si II	49	4	12.58	0.05
177			Si III	151	5	13.01	0.02
178			Si IV	61	4	12.88	0.04
179			C II	82	4	13.67	0.03
180	SBS1108+560	0.002	C IV	56	5	13.20	0.05
181			H I	548	15		
182			Si II	112		11.92	
183			Si III	90	11	12.67	0.07
184			Si IV	89	12	13.01	0.09
185	SBS1122+594	0.060	C II	33	11	13.21	0.14
186			C IV	404	13	14.22	
187			H I	1790	193		
188			Si II	464	65	13.44	
189			Si III	690	76	13.66	
190	SBS1122+594	0.004	Si IV	450	18	13.92	
191			C II				
192			C IV	758	26	14.58	
193			H I	659	23		
194			Si II	36	11	12.48	0.17
195	SBS1122+594	0.004	Si III	83	12	12.68	0.11
196			Si IV	54	13	12.85	0.14
197			C II	145	13	13.92	0.07
198			C IV	75	20	13.33	0.18
199			H I	805	20		
200	SDSS-J093001.90+284858.4	0.023	Si II	118		12.16	
201			Si III	275	19	13.32	
202			Si IV	121	21	13.28	0.08
203			C II	96	21	13.78	0.11
204			C IV	572	27	14.49	0.03
205	SDSS-J124129.64+285212.0	0.067	H I	4236	387		
206			Si II	555	78	13.57	
207			Si III	568	51	13.53	
208			Si IV	225	59	13.64	0.09
209			C II	648	55	14.66	
210	SDSS-J124129.64+285212.0	0.067	C IV				
211			H I	1794	59		
212			Si II	479	34	13.80	
213			Si III	474	32	13.60	
214			Si IV				
215			C II	577	36	14.63	
216			C IV				

Table A.8. Absorption-line systems - part IV

No.	QSO (COS name)	z_{abs}	Ion	W_r [mÅ]	ΔW_r [mÅ]	$\log N$	$\Delta(\log N)$
217	SDSS-J150928.29+070235.7	0.079	H I	916	28		
218			Si II	140	35	13.07	0.11
219			Si III	177	23	≤ 13.11	
220			Si IV				
221	SDSS-J151237.05+012846.	0.029	C II	79	33	13.77	0.13
222			C IV				
223			H I	4319	351		
224			Si II	1077	76	≤ 14.13	
225	SDSSJ004222.29-103743.8	0.095	Si III	582	80	≤ 13.66	
226			Si IV	j82		≤ 13.58	
227			C II	861	76	≤ 14.91	
228			C IV				
229	SDSSJ080908.13+461925.6	0.047	H I	1424	48		
230			Si II	249	28	≤ 13.37	
231			Si III	590	30	≤ 13.63	
232			Si IV	305	39	≤ 13.67	
233	SDSSJ082633.51+074248.3	0.051	C II	295	26	≤ 14.29	
234			C IV	615	67	≤ 14.24	
235			H I	1026	22		
236			Si II	j13		≤ 12.11	
237	SDSSJ084349.49+411741.6	0.030	Si III	39	7	12.33	0.13
238			Si IV	j51		≤ 12.82	
239			C II	11	5	12.78	0.25
240			C IV	61	17	13.26	0.24
241	SDSSJ092909.79+464424.0	0.065	H I	1070	27		
242			Si II	j40		≤ 12.68	
243			Si III	172	25	13.02	0.09
244			Si IV	j20		≤ 12.52	
245	SDSSJ094952.91+390203.9	0.018	C II	213	25	≤ 14.14	
246			C IV	456	56	≤ 14.23	
247			H I	418	33		
248			Si II	j105		≤ 12.92	
249	SDSSJ095109.12+330745.8	0.005	Si III	65	31	12.64	0.25
250			Si IV	j30		≤ 12.70	
251			C II				
252			C IV	161	37	≤ 13.88	
253	SDSSJ100902.06+071343.8	0.059	H I	251	17		
254			Si II	46	12	12.56	0.15
255			Si III	37	11	12.32	0.16
256			Si IV	j10		≤ 12.26	
257	SDSSJ100902.06+071343.8	0.059	C II	34	7	13.26	0.15
258			C IV				
259			H I	831	23		
260			Si II	j23		≤ 12.31	
261	SDSSJ105915.65+050355.1	0.059	Si III	169	25	13.01	0.08
262			Si IV	75	25	13.07	0.14
263			C II				
264			C IV	638	43	≤ 14.48	
265	SDSSJ105915.65+050355.1	0.059	H I	1308	1106		
266			Si II	534	35	≤ 13.92	
267			Si III	615	62	≤ 13.65	
268			Si IV	328	83	≤ 13.81	
269	SDSSJ100902.06+071343.8	0.059	C II	481	44	≤ 14.52	
270			C IV				
271			H I	1066	33		
272			Si II	572	20	≤ 13.76	
273	SDSSJ100902.06+071343.8	0.059	Si III	566	21	≤ 13.71	
274			Si IV	301	32	13.64	0.07
275			C II	542	8	≤ 14.69	
276			C IV	875	41	≤ 14.56	
277	SDSSJ105945.23+144142.9	0.002	H I	1711	64		
278			Si II				
279			Si III	182	36	≤ 13.00	
280			Si IV	j30		≤ 12.74	
281	SDSSJ105945.23+144142.9	0.002	C II	104	19	13.80	0.15
282			C IV	210	55	13.90	0.18
283			H I	639	28		
284			Si II	j31		≤ 12.44	
285	SDSSJ105945.23+144142.9	0.002	Si III	125	22	12.97	0.12
286			Si IV	j34		≤ 12.76	
287			C II	47	11	13.50	0.18
288			C IV	203	20	≤ 13.93	

Table A.9. Absorption-line systems - part v

No.	QSO (COS name)	z_{abs}	Ion	W_r [mÅ]	ΔW_r [mÅ]	$\log N$	$\Delta(\log N)$
289	SDSSJ110406.94+314111.4	0.062	H I	538	28		
290			Si II	118		12.16	
291			Si III	25	8	12.17	0.19
292			Si IV	121		12.46	
293			C II	19	8	13.00	0.20
294	SDSSJ111239.11+353928.2	0.025	C IV	279	34	14.04	
295			H I	955	52		
296			Si II	146	44	13.18	0.14
297			Si III	267	73	13.31	0.10
298			Si IV	69	35	13.18	0.14
299	SDSSJ111754.31+263416.6	0.048	C II	190	28	14.18	0.08
300			C IV	260	158	14.01	0.01
301			H I	818	35		
302			Si II	223	22	13.33	
303			Si III	270	19	13.31	
304	SDSSJ121037.56+315706.0	0.060	Si IV	152	19	13.34	0.08
305			C II	338	23	14.44	
306			C IV	425	59	14.24	
307			H I	540	44		
308			Si II	182	44	13.30	0.13
309	SDSSJ121037.56+315706.0	0.060	Si III	146	26	12.91	
310			Si IV	137	29	13.28	0.12
311			C II	122	19	13.87	0.10
312			C IV	283	34	14.02	
313			H I	529	26		
314	SDSSJ133053.27+311930.5	0.089	Si II	132		12.33	
315			Si III	19	11	12.13	0.21
316			Si IV	113		12.28	
317			C II				
318			C IV	37	17	13.13	0.27
319	SDSSJ133053.27+311930.5	0.034	H I	810	27		
320			Si II	48	26	12.75	0.16
321			Si III	242	22	13.21	0.07
322			Si IV	140	26	13.26	0.09
323			C II	78	20	13.67	0.17
324	SDSSJ134246.89+184443.6	0.085	C IV	389	41	14.21	
325			H I	637	30		
326			Si II	111		11.87	
327			Si III	163	27	12.99	0.07
328			Si IV	121		12.54	
329	SDSSJ134246.89+184443.6	0.027	C II				
330			C IV	96	16	13.38	0.11
331			H I	499	31		
332			Si II	169		12.80	
333			Si III	39	15	12.47	0.17
334	SDSSJ134251.60-005345.3	0.088	Si IV	27	10	12.63	0.15
335			C II				
336			C IV	80	21	13.43	0.22
337			H I	698	38		
338			Si II	125		12.29	
339	SDSSJ134251.60-005345.3	0.071	Si III	58	22	12.55	0.21
340			Si IV	130		12.72	
341			C II				
342			C IV	121	38	13.65	0.16
343			H I	745	57		
344	SDSSJ135712.61+170444.1	0.098	Si II	275	28	13.41	0.07
345			Si III	402	29	13.43	
346			Si IV	568	35	14.02	
347			C II	369	29	14.38	
348			C IV	361	52	14.08	
349	SDSSJ135712.61+170444.1	0.084	H I	992	26		
350			Si II	69	13	12.69	0.11
351			Si III	352	18	13.39	
352			Si IV	166	42	13.33	0.10
353			C II	117	18	13.78	0.09
354	SDSSJ135712.61+170444.1	0.084	C IV	324	58	14.03	0.08
355			H I	1190	28		
356			Si II	115		12.16	
357			Si III	286	51	13.30	
358			Si IV	77	18	12.99	0.12
359	SDSSJ135712.61+170444.1	0.084	C II	48	16	13.44	0.12
360			C IV	358	59	14.12	

Table A.10. Absorption-line systems - part VI

No.	QSO (COS name)	z_{abs}	Ion	W_r [mÅ]	ΔW_r [mÅ]	$\log N$	$\Delta(\log N)$
361	SDSSJ140732.25+550725.6	0.005	H I	3422	89		
362			Si II	550	17	$\log 13.93$	
363			Si III	769	21	$\log 13.85$	
364			Si IV	294	27	$\log 13.67$	
365			C II	610	19	$\log 14.75$	
366			C IV				
367	SDSSJ141542.90+163413.8	0.008	H I	3267	376		
368			Si II	221	20	13.34	0.05
369			Si III				
370			Si IV	123	20	13.25	0.09
371			C II	273	22	$\log 14.32$	
372			C IV				
373	SDSSJ152139.66+033729.2	0.097	H I	1047	46		
374			Si II	114		$\log 12.05$	
375			Si III	61	32	12.62	0.26
376			Si IV	75		$\log 13.06$	
377			C II	43	26	13.64	0.15
378			C IV	246	45	$\log 13.67$	
379	SDSSJ155304.92+354828.6	0.083	H I	2827	93		
380			Si II	299	24	$\log 13.54$	
381			Si III	372	37	$\log 13.41$	
382			Si IV	188	26	$\log 13.39$	
383			C II	300	21	$\log 14.38$	
384			C IV	307	45	$\log 14.04$	
385	SDSSJ161916.54+334238.4	0.096	H I	4849	229		
386			Si II	254	25	$\log 13.43$	
387			Si III	296	33	$\log 13.30$	
388			Si IV	87	10	13.04	0.08
389			C II	356	18	$\log 14.36$	
390			C IV	258	39	13.90	0.09
391	UKS-0242 $\log 124$	0.064	H I	940	20		
392			Si II	127	10	12.96	0.04
393			Si III				
394			Si IV	115		$\log 12.43$	
395			C II	78	18	13.67	0.08
396			C IV				
397	VIIZW244	0.002	H I	611	14		
398			Si II	24	7	12.30	0.15
399			Si III	148	8	13.02	0.04
400			Si IV	47	6	12.77	0.09
401			C II	44	7	13.40	0.09
402			C IV	83	10	13.42	0.09
403	VV2006-J015953.0+134554	0.044	H I	1605	31		
404			Si II	174	36	13.23	0.15
405			Si III	324	16	$\log 13.49$	
406			Si IV	120		$\log 12.52$	
407			C II	364	31	14.44	0.09
408			C IV				
409	VV2006-J080838.8+051440	0.029	H I	803	33		
410			Si II	104	18	13.00	0.16
411			Si III	188	21	$\log 13.18$	
412			Si IV	44		$\log 12.87$	
413			C II	184	37	$\log 14.15$	
414			C IV				
415	VV2006-J112005.0+041323	0.050	H I	918	43		
416			Si II	176	43	$\log 13.33$	
417			Si III	160	25	$\log 13.02$	
418			Si IV	131		$\log 12.73$	
419			C II	332	40	$\log 14.47$	
420			C IV				
421	VV2006-J130524.3+035731	0.001	H I	2468	32		
422			Si II	283	16	$\log 13.53$	
423			Si III	329	20	$\log 13.44$	
424			Si IV	31	16	12.68	0.21
425			C II	367	21	$\log 14.55$	
426			C IV				

Table A.12. Comparison with (revised) Danforth et al. (2016) absorber list

QSO (COS name)	z_{abs}	Comment
Danforth detections without Richter counterpart		
3C57	0.077417	many line blends
3C57	0.089742	candidate metal lines are offset from Ly α
MR2251-178	0.010725	candidate metal lines are offset from Ly α
RXJ1230.8+0115	0.071728	no evidence for metal absorption
Richter candidate system without Danforth counterpart		
RXJ0439.6-5311	0.057400	possible Si III absorber present, but blend with intrinsic Ly β